Degradation of NiTi springs through electronic actuation

Sævar Örn Einarsson

Final Report in Mechanical Engineering B.Sc.

2016

Name: Sævar Örn Einarsson
Kennitala: 120392-2209
Supervisor: Joseph T. Foley

School of Science and Engineering
Tækni- og verkfræðideild

Heiti verkefnis:

Degradation of NiTi springs through electronic actuation

Námsbraut:

Mechanical Engineering B.Sc.

Tegund verkefnis:

Final Report in Tæknifræði B.Sc.

Önn:

2016–2

Námskeið:

VT LOK 1012

Höfundur:

Sævar Örn Einarsson

Umsjónarkennari:

Indriði Sævar Ríkharðsson

Leiðbeinandi:

Joseph T. Foley

Fyrirtæki/stofnun:

Háskólinn í Reykjavík
Menntavegur 1
101 Reykjavík

Ágrip:

Shape Memory Alloys (SMA) have the unique ability to recover its shape when heated. NiTi is a common SMA that is used mainly in orthodontic wires and light actuators such as on the NASA Pathfinder. However, when used in springs, the long-term reliability of these actuation forces has rarely been investigated. As SMAs are non-ferrous, it can be deduced that some structural degradation occurs Due to SMA NiTi's high electrical resistance, actuation is most convenient through resistive heating. Therefore, this thesis evaluates the degradation of the consequent actuation force through electronic heating over the expected lifetime of 10.000 cycles. Results showed exponential decay with a maximum 6% force degradation over 10.000 iterations.

Dagsetning:

19 August 2016

Lykilorð íslensk:

Lykilorð ensk:

Dreifing:

opin ☐   **lokuð** ☐   **til:**

The undersigned hereby grants permission to the Reykjavík University Library to reproduce single copies of this Final Report entitled **Degradation of NiTi springs through electronic actuation** and to lend or sell such copies for private, scholarly or scientific research purposes only.

The author reserves all other publication and other rights in association with the copyright in the Final Report, and except as herein before provided, neither the Final Report nor any substantial portion thereof may be printed or otherwise reproduced in any material form whatsoever without the author's prior written permission.

....
date

....
Sævar Örn Einarsson
Bachelor of Science

Acknowledgements

Contents

List of Figures

List of Tables

Chapter 1

Introduction

Since the advent of the combustion engine and the dawn of the industrial age, material scientists have striven towards developing more suitable materials (harder, stronger and more heat- as well as corrosion-resistant) for more challenging mechanical applications. This development has led to the discovery of materials that themselves can be used as actuators, classified as "smart materials". Smart materials can be sensors or actuators, some even acting as both. There are four types of materials that are commonly used as actuators: Shape-memory alloys, piezoelectric ceramics, magnetostrictive materials, and electrorheological/magnetorheological fluids. The first of which is the focus of this work. [1]

Shape Memory Alloys (SMA) are an excellent example of the variety of these varying applications. They are metal alloys that have the ability to recover their shape when heated to a specific temperature. This feature can be effectively utilized in many different ways as it provides a useful actuation force with an extremely low net volume and no additional moving parts. With the increasing need for smaller actuators, the industry has been exploring new methods and materials. SMAs have seen uses in pipe couplings, aerospace, various medical applications and actuating the solar panel on the NASA Pathfinder rover (Section 1.2.4). [2]

A popular SMA is the NiTi alloy, commercially known as Nitinol. It is most common due to its high electrical resistance, resulting in easy heating of the material through electric current. In addition, it has high biocompatibility and super-elasticity giving it excellent application possibilities in the medical field. Due to these characteristics, the use of Nitinol is the main focus of this thesis.

1.1 Background

In the 1890s, Adolf Martens gained significant prestige by discovering a crystalline phase transformation in steels, which has been known as martensite. With the prospect of greatly strengthening steels by heat treatment, the martensitic transformation to austenite and back became one of the most widely studied metallurgical phenomenon in the early 1900s. During that period, the Fe-C system was observed and the phase transformation process was established as irreversible. However, the effect was later found to be reversible in alloys such as InTl and CuZn. [3]

In 1956, William Buehler at the Naval Ordnance Laboratory (NOL) supervised research into heat-resistant alloys for weapon development. In his research, he noted a difference in the sounds that Ti-Ni bars made at different temperatures, suggesting a phase change. A use for that effect was never implemented in engineering applications until Buehler's eventual public disclosure in 1964 regarding shape memory. As with many discoveries, it was seemingly by

Alloy	Composition	Transition Temp. (°C)	Hysteresis (°C)
AgCd	44/49 wt% Cd	[-190,-50]	15
AuCd	46,5/50 wt% Cd	[30,100]	15
CuAlNi	14/14,5 wt% Al, 3/4,5 wt% Ni	[-140,100]	35
Cu-Sn	15 wt% Sn	[-120,30]	10
CuZn	38,5/41,5 wt% Zn	[-180,-10]	10
CuZnX (X=Si, Sn, Al)	few wt% of X	[-180,200]	10
InTi	18/23 wt% Ti	[-60,100]	4
NiAl	36/38 wt% Al	[-180,100]	10
NiTi	49/57 wt% Ni	[-50,110]	30
FePt	Approx. 25 wt% Pt	Around -130	40

Table 1.1: Different alloys showing SMA characteristics. Reproduced from [4]

	NiTi	CuZnAl	CuAlNi
Maximum temperature shape recovery (°C)	100	120	200
Maximum recoverable strain (%)	8	6	5
Hysteresis (°C)	12-50	10-25	15-20
Austenite yield stress (MPa)	415	350	400
Martensite yield stress (MPa)	70	80	130
Break stress (MPa)	700	600	500-800
Density (g/cm^3)	6,05	7,6-8,0	7,02
Resistivity (μΩ cm)	80-90	8,5-9,7	11-13
Thermal capacity (J/kgK)	837	400	373-574

Table 1.2: Comparison between NiTi, CuZnAl, and CuAlNi SMAs. Reproduced from [4]

chance that the shape memory effect derived from this reversible phase change was observed. [4]

At an administrative meeting in 1962, Buehler passed around a wire to demonstrate its resistance to cyclic loading. One pipe smoker asked the question of how it would resist heating, while bringing the wire to his lighter and, to the astonishment of everyone present, the wire straightened. Subsequently, Buehler coined the name Nitinol for the alloy, derived from the alloy itself (NiTi) and the institution that it was discovered in (NOL). Much research went into finding a commercial use for this phenomenon but none would present itself for some years. [4]

Since that initial observation, multiple SMAs have been discovered (Table 1.1). In terms of workability, yield strength, and resistivity, NiTi has been most popular (Table 1.2). NiTi has 8 times more electrical resistance and more than double the thermal capacity compared to similar SMAs.

1.2   Characteristics of SMAs

The Shape Memory Effect (SME) is the intrinsic ability of SMAs to remember their shape. In essence, it is the reversible solid-solid transformation from low-temperature martensite to high-temperature austenite. The transformation between these phases occurs by shear lattice

(a) Macro- and Microscopic view   (b) Temperature-load plot
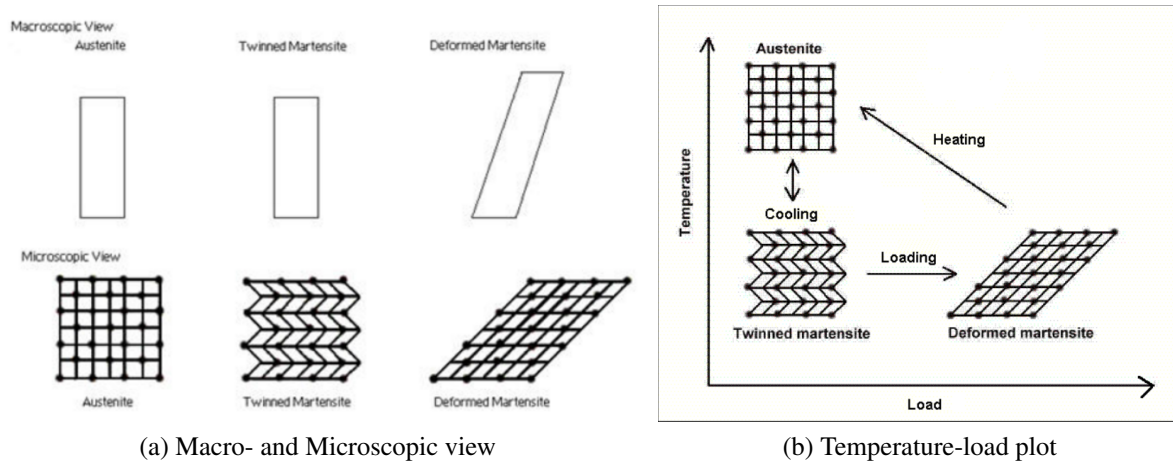
Figure 1.1: The crystalline transformation that occurs in the NiTi phase change [5].

distortion where the crystalline structure follows a cubic structure for martensite and tetragonal for austenite.

Each crystal structure can be oriented in a different way, called a variant of the martensite phase. The phase exists in two forms; twinned and detwinned martensite. When one variant assembly is dominant the material is said to be detwinned (M^d) and when the structure is formed by a combination of "Self accommodated" martensitic variants, it's said to be twinned (M^t). [3]

When the material is cooled in the absence of an applied load, the austenite to martensite transformation results in a twinned martensite. This is known as a forward transformation and it results in the formation of multiple martensitic variants, up to 24 for NiTi. When yield strain is applied to the material, it deforms into detwinned martensite and retains its shape after the load is released. At this point, heating the material above a set temperature results in a reverse phase transformation directly from detwinned martensite to austenite. Finally, cooling will result in a direct transformation to twinned martensite as seen in Figure 1.2. [3]

1.2.1 One-way shape memory effect

The one-way SME is when the material returns to the austenite shape when heated but requires an externally applied mechanical load for it to return to a detwinned martensitic state[3]. Due to the lower level of processing needed for the material and therefore cost, this effect is the most adopted in modern applications. An as-drawn SMA wire is initially in its martensitic phase and the element in a relaxed state, given that it's maintained at a relatively constant temperature. When the material temperature is increased (exact temperature different for each alloy) the austenite phase will begin to appear and, if designed for, produce work. When cooled, the element has not completed a full actuation cycle until a mechanical load is applied to deform it back to the detwinned martensite. [6]

This effect can prove useful for other applications such as temperature sensitive actuators, retrievable medical implants and novelty items such as seen in Figure 1.4 [4]. It is shown in Figures 1.2 and is the subject of this thesis since the NiTi springs display a conventional one-way SME as seen in Figure 1.3.

Figure 1.2: Stress-strain-temperature plot showing the cycle of the SME in a typical NiTi sample. [3]

Figure 1.3: The resultant SME from actuation of a NiTi spring. [7]

(a) Fan driven with heat   (b) HOT SMA lettering
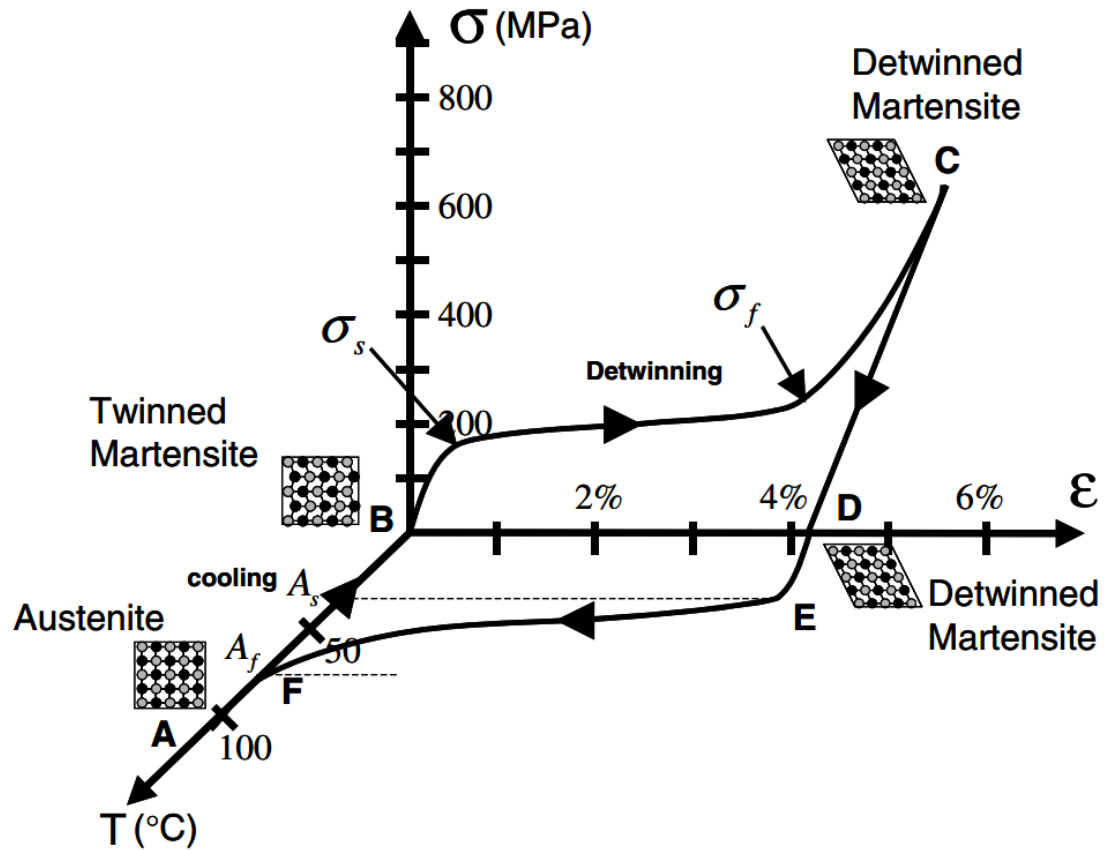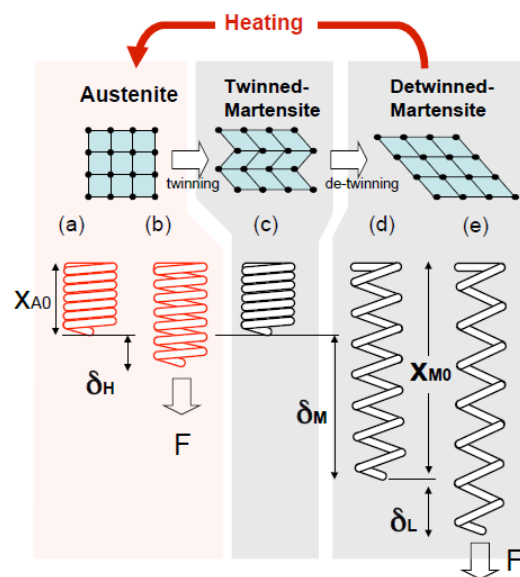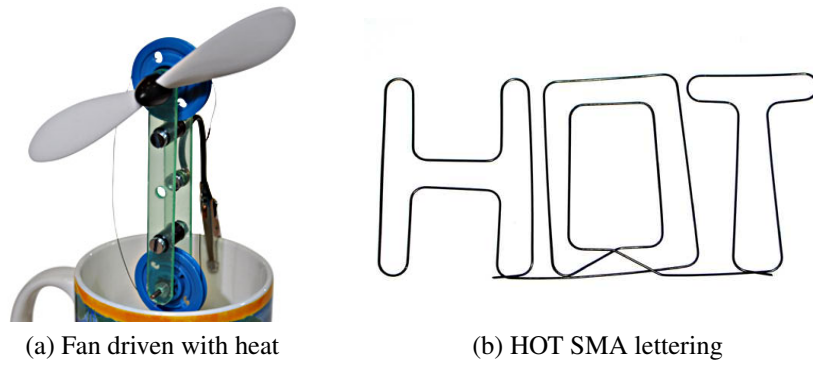
Figure 1.4: Novelty items sold by Grand Illusions Ltd. using Nitinol wires [8]

1.2.2 Two-way shape memory effect

The two-way SME (TWSME) is when the material exhibits a shape change during both heating and cooling, returning to the detwinned martensite shape when cooled without any additional mechanically applied load [4]. This is often applied in order to dismiss a biasing force entirely, but cannot be used to apply a force both ways [6]. TWSME occurs in a SMA material after it has been subjected to repeated thermo-mechanical cycling along a specific loading path, known as training. If performed correctly, this repetition changes the microstructure, which induces macroscopically observable modifications, or the TWSME. [3]

Another case of the TWSME is the All-round SME, showing a greater amount of shape change and force actuation both ways. In addition, the high-temperature austenite shape is a direct inverse of the low-temperature detwinned martensite phase that it shows when cooled [9]. This can be specifically useful when dealing with mirrored applications since the low and high-temperature shapes are complete opposites. However, this effect is rarely used as it is hard to acquire [6].

1.2.3 Previous Applications

After the initial discovery of Nitinol, many funded research efforts were incited, with varying levels of success. It was first used commercially in a pipe coupling in the early 1970s. The material would be machined into a hollow cylinder with an inner diameter smaller than the pipes to be coupled, then cooled with liquid nitrogen and made to reach its permanent austenite phase when in place. Despite high expenses, this method of coupling is still considered cutting-edge in the industry and sparked many different uses. [4]

Due to its excellent biocompatibility, Nitinol does not corrode in biological surroundings, so it has been exceedingly popular for use in orthodontic wires. In 1972, Unitek Corporation (now, 3M Unitek) started production of a commercial Nitinol wire (Ni 55% wt) to be used in clinical applications. The wire does not use shape memory but was nonetheless used for its advantage in lighter installation forces and an overall larger spring-back. [4]

In addition, the use of Nitinol has been popular in novelty items to be used in mid-level science classes, such as the fan and lettering in Figure 1.4. Since its discovery, Nitinol has seen many different applications in various fields and the possible applications have often been thought to be beyond count. However, the lack of data representing the reliability of cyclic loading begs the question how the material degrades over time, particularly when electrically actuated.

1.2.4   Springs or Linear actuators

When SMAs are used for commercial actuation, the more common application is a so-called muscle wire. Instead of showing a SME, the wire stretches and retracts on demand. This is certainly useful for many applications, but often results in lower magnitude strains and a lower level physical change. Therefore, muscle wires often require a mechanism with large cam systems or lever arms in order to get the desired level of actuation. One example of this is the NASA Pathfinder rover [2], where a rotating axle was used to operate a cover glass over the solar cell for the rover. A NiTi muscle wire was wrapped around the axle to achieve the required 32° rotation to uncover the solar cell.

Very little research has explored SMA springs as actuators as it has been regarded as a more difficult subject to address, but the possibilities are apparent. Kim et al. [7] produced a more accurate model of the NiTi spring as an actuator, where a procedure was presented to manufacture the springs.

1.3   Objective

Despite many different applications that have been implemented for various types of SMAs, there is still a question of how well they resist degradation when repeatedly actuated. The objective of this thesis is to produce data that will work as a proof of concept for the reliability of SMA springs as cyclic actuators. The question becomes, "How much do shape memory spring actuators degrade over their lifetime?".

Chapter 2

Methods

The objective of this thesis is to conduct a mechanical cycling experiment to obtain quantifiable data evaluating the cyclic degradation of the tensional force generated when heating an SMA spring. An effective automatic test system must be developed that can repeatably perform consecutive heating and cooling of a wide variety of SMA springs and accurately measure the resultant tensional force.

Preliminary measurements show that the spring constant of Nitinol springs in the high temperature austenite phase is 2-3 times larger than in the lower temperature martensite phase. Predki et al. [10] showed that cylindrical SMA specimen (tubes and shafts) experience cyclic ruptures between 3.201 and 19.188 cycles when actuated with frequencies ranging from 0,1 to 1,0 Hz. Basing on that range, it is assumed that a trend will be definitive after 10.000 actuations.

Therefore, the aim is to conduct 10.000+ actuation cycles of each specimen in order to acquire a reliable set of data to confirm the level and development of the force degradation with regard to cycles actuated. This chapter explains the development of the system required to gather the relevant SMA spring degradation data.

2.1 Preliminary Considerations

2.1.1 Manufacture Procedure

The procedure followed here is similar to that described by Kim et al. [7], where a wire is guided onto a . When winding the springs, a fishing reel is used to feed the wire onto a rotating core rod, matching the inner diameter goal. Kim et al. [7] show that more deformation happens when the springs are annealed at temperatures over $400C$, maintaining reasonable consistency a lower temperatures. Working on that principle, each spring tested is wound and annealed at $400C$ for 15 minutes.

2.1.2 Force Range

At first, it is necessary to define the range of forces that are going to be dealt with. The available wire diameters for springs are two extremes in this application, or $D_1 = 0,1908$mm and $D_2 = 0,82$mm. To acquire universal testing equipment, it is necessary for it to be able to handle the full range of forces possible with these two diameters. After initial testing it was determined that the range of actuation forces would be $0,49 - 24$N, equivalent to a mass of $0,05 - 2,45$kg.

2.2   Mechanical Design

Employing the methodology known as Axiomatic Design and its axioms, the next step is to define a set of Functional Requirements (FRs) and Design Parameters (DPs) to simplify the design process [11]. The FRs typically begin with an action verb and act as independent minimum requirements that represent the objective an ideal design would fulfill. DPs normally start with a noun and help identify the physical characteristics that address their subsequent FRs. Here, FRs and DPs are assessed using the Independence Axiom (Axiom 1) which entails the maintenance of independence in each FR, and that each DP should be adjusted to satisfy its FR without affecting other FRs. [12] However, in this setting, it is best to first define a set of constraints that are crucial for the successful completion of this research. They are the following:

C_1 Total time of 12 weeks.

C_2 Budget of 50.000 ISK.

C_3 Dimensions suitable for a desktop setup.

To keep each phase in accordance with the correct process, complete cycles of FR-DP mapping are performed before returning to the upper levels. This is known as "zig-zagging" through the domains. Working with these principles and with the constraints in mind, the following top-level primary FR is defined:

FR_0 Measure force generated by spring.

Consequently, a guiding concept DP_0 is generated:

DP_0 Frame around strain gauge.

FRs should be defined in a way that states what is required without providing the means to accomplish it (solution neutrality) [12]. As there are only basic requirements to be stated, the following is defined:

FR_1 Transmit force from actuator to strain gauge.

FR_2 Measure force.

Once the necessary FRs have been generated, they must each be addressed by producing independent physical solutions, or DPs:

DP_1 Actuator directly connected between strain gauge and an adjustable square frame.

DP_2 VPG Transducers load cell model 1006. 0-2000g range.

Considering the above FRs and DPs, a design matrix (Figure 2.1) is an excellent way to represent them visually. The design matrix works as a tool to evaluate how each FR affects each DP. If each FR only affects its respective DP, the matrix is or diagonal. A matrix that is diagonal is said to be "uncoupled", but "decoupled" if it is triangular, and coupled in any other form. When a design matrix is coupled, there is no way to know if a feasible solution exists that satisfies all FRs in an efficient manner [12]. This led to defining the uncoupled first design matrix shown in Figure 2.1. [11]

	DP1: Actuator directly connected between strain gauge and frame	DP2: VPG transducers load cell model 1006. 0-2000g range
FR1: Transmit force from actuator to strain gauge	X	
FR2: Measure force		X
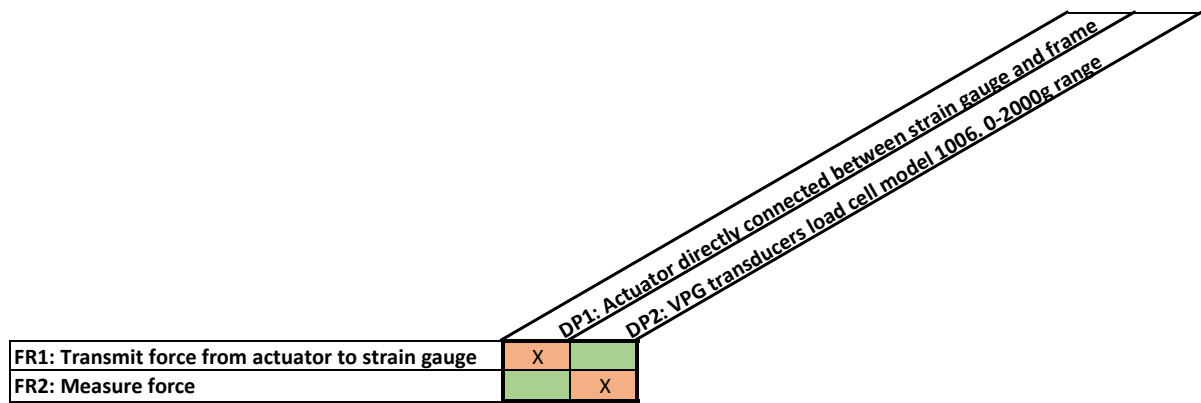
Figure 2.1: Design matrix 1 for the adjustable square frame concept.

2.2.1 Adjustable square frame

The first concept investigated for a test frame was a rectangular frame with an SMA spring mounted between two adjustable square plates. This could easily be set to desired height to reach a set level of initial tension (see Figure 2.2). However, this setup was found to be non-ideal since springs produce between 0,49-24N (equivalent to a mass of 0,05-2,45kg) tensional force and the most suitable load cell available has a capacity of only 2kg [13].

Figure 2.2: First concept with an adjustable square frame around the strain gauge.

2.2.2 Lever arm

At this point, it is relatively simple to revise preliminary design concepts and strategically improve the results. Returning to the FRs and DPs, the FRs remain the same but the following DPs are redefined:

DP$_1$ Lever arm between actuator and strain gauge.

DP$_2$ VPG Transducers load cell model 1006. 0-2000g range.

These revised DPs resulted in a second version of the design matrix (Figure 2.3). Here, a revised design was implemented where the resultant tensional force from the springs could be scaled by a factor of 20 both ways. This scaling could be easily tuned by moving the load cell and/or spring mounting in either direction along the base profile in order to meet the desired force range. In addition, the height could easily be tuned to accommodate differing spring length as seen in Figure 2.4.

	DP1: Lever arm between actuator and strain gauge	DP2: VPG transducers load cell model 1006. 0-2000g range
FR1: Transmit force from actuator to strain gauge	X	
FR2: Measure force		X
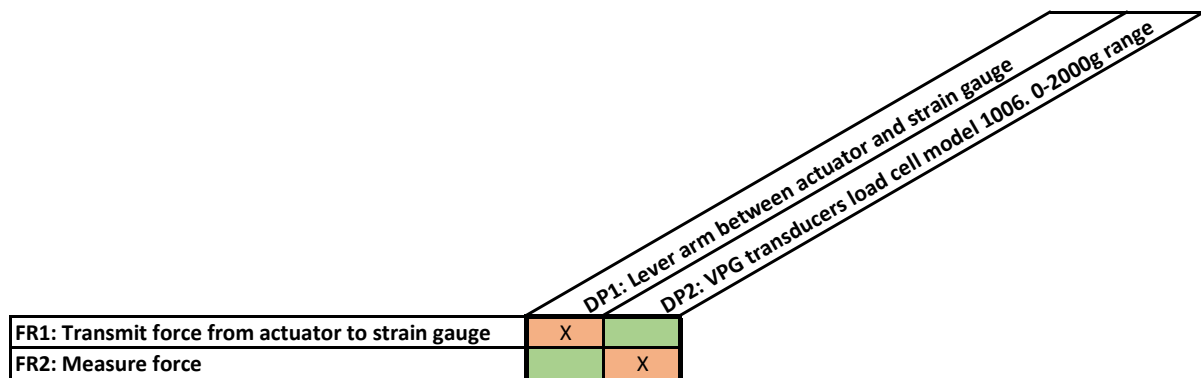
Figure 2.3: Design matrix 2 addresses the limited load cell capacity.
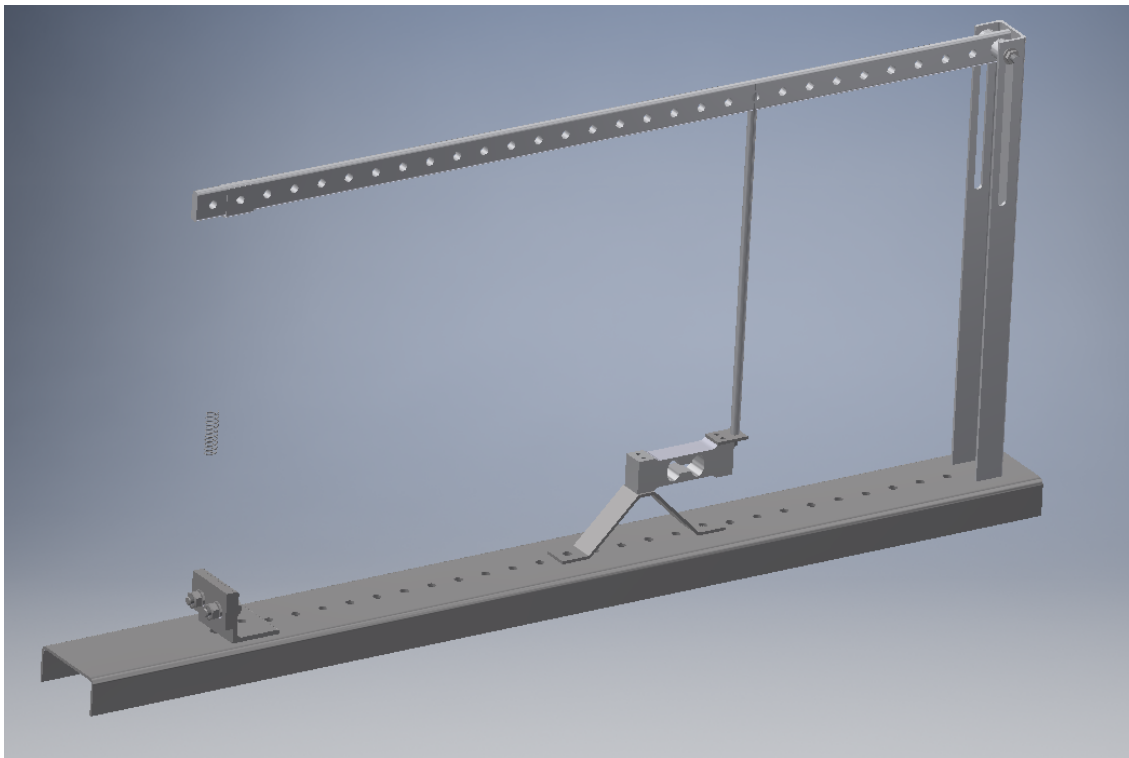
Figure 2.4: Lever arm setup, fulfilling all requirements in the design matrix.

2.2.3 Aluminum profiles

To allow for incremental scaling and a more rapid construction, the previously mentioned setup was built from standard aluminum extrusion profiles supplied by MiniTec [14]. These profiles, seen in Figure 2.5 and listed in Table 2.1, allow for excellent adaptive scaling of the forces seen in Figure 2.6. This is achieved through extruded ridges in these profiles, making the design lightweight, with easily threaded ends as well as custom nuts and hinges. Additionally, rubber feet were added to the frame to ensure good isolation from possible surrounding vibration.
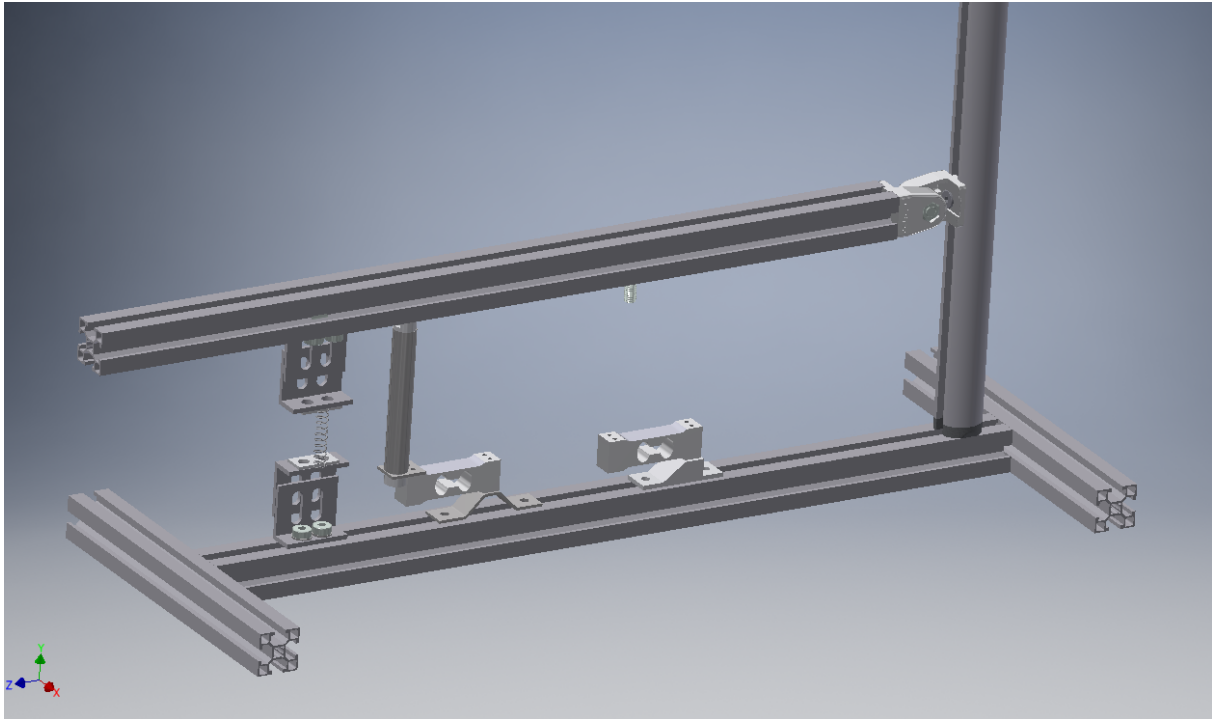
Figure 2.5: Test setup with profiles from Minitec [14] and two different load cell mounting methods.
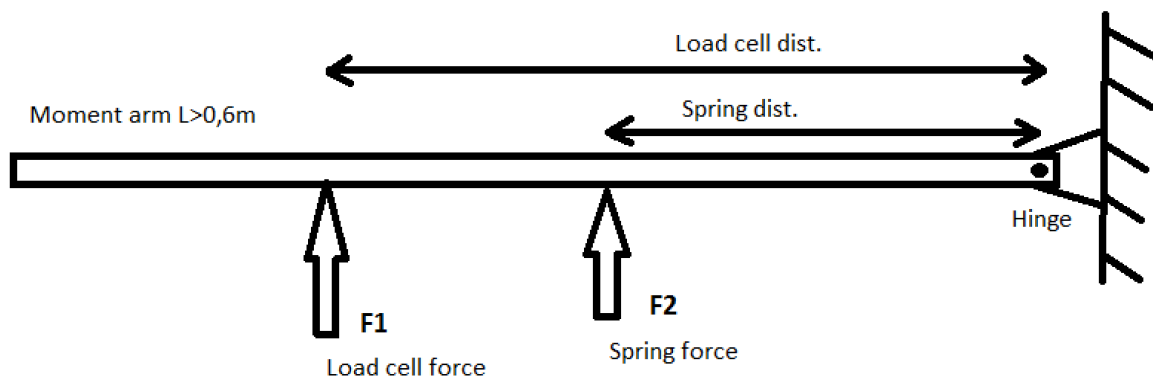
Figure 2.6: The resultant force diagram for the employed in the setup with an adaptive lever arm.

2.2.4   Carbon tube for lever arm

The scaling of the force can be described with a simple lever arm equation based on Figure 2.6
  Because this is in equilibrium, the torque of the system can be described with system torque (τ) from the Load cell (τ_c), spring (τ_s), and lever arm (τ_L).

$$\tau = \tau_c - \tau_s - \tau_L = 0 \tag{2.1}$$
$$\tau_c = \tau_s + \tau_L \tag{2.2}$$

They can further be described with the following:

$$\tau_s = L_s F_s \tag{2.3}$$
$$\tau_L = \frac{m_L L_L g}{2} \tag{2.4}$$
$$\tau_c = L_c F_c \tag{2.5}$$

where, $L_s = 0.42\,\text{m}$ is the displacement between the spring and pivot point, F_s is the force from the spring, m_L is the mass of the lever arm, L_L is the total length of the lever arm, L_c is the length between Load cell and pivot point, and F_c is the force onto the Load cell. We can now derive the relationship between F_c and the rest of the parameters:

$$F_c = \frac{L_s F_s + \frac{m_L L_L g}{2}}{L_c} \tag{2.6}$$

From the load cell specifications, the maximum force ($F_{c,max}$) that it can measure safely:

$$F_c \leq F_{c,max} = (2\,\text{kg})(9.81\,\text{m s}^{-2}) = 19.62\,\text{N} \tag{2.7}$$

  Despite using the very light aluminum extrusions, the lever still had a mass of $m_L = 0,378\text{kg}$. This resulted in limited force amplification since the load cell (according to Equations 2.6 & 2.7 with the profile mass) would surpass maximum capacity ($m_L = 2\text{kg}$), no closer than $L_c = 61\,\text{mm}$ from the hinge point, resulting in a maximum force amplification factor just under 10, and virtually no allowable actuation force at that point.
  Therefore, a carbon tube ($D_{outer} = 10.01\,\text{mm}$, $D_{inner} = 7.3\,\text{mm}$) was chosen to replace the aluminum extrusion lever, weighing only $m_L = 0.0509\,\text{kg}$ while maintaining sufficient stiffness. Using this much lighter carbon tube, the load cell would only measure $m_L = 0.65\,\text{kg}$ at the closest point possible to the load cell, leaving enough capacity to measure a force scaled by a factor of 24. This is also a much lower information content design, as it can handle a larger force range and meets all the current needs. As Suh states: "If the task is so configured that it can always be satisfied without any prior knowledge or additional knowledge, then the probability of success is unity while the requisite information is zero." [11, page 149]. Therefore, it complies much better with the second axiom, as there is virtually no information being transmitted other than what is relevant to the design and demanded by the FRs. This final design can than be said to include an information content of zero. Figure 2.7 shows the final design with a carbon tube as a lever arm and custom built fixtures. [11]

2.3   Data Acquisition

Multiple means of data acquisition (DAQ) are possible for this kind of system. The cheapest to implement would be an Arduino microprocessor (40 USD) to obtain force measurements.

Item	Supplier	Part no.	Size/Length	Quantity
Profile 30x30	MiniTec	201068/0V	0,6 m	1
Profile 30x30	MiniTec	201068/0V	0,25 m	2
Handle profile 32	MiniTec	201088/0V	0,5 m	1
Power lock fastener 30 SF	MiniTec	210016/0	N/A	3
Square-Nut 30 M08	MiniTec	211570/0	N/A	6
Hex socket cap screw M08x10	MiniTec	211686/0	N/A	6
Adapter 30x30 / G 32	MiniTec	210953/0	N/A	1
End cap 30x30 Z grey	MiniTec	221146/1	N/A	5
End cap handle profile 32 Z	MiniTec	221162/1	N/A	1
Stopper 30	MiniTec	211759/1	N/A	4
Link 30 F/S	MiniTec	212105/0	N/A	1
Pultruded Carbon Tube	Goodwinds	100130	0.914 m	1
Solenoid Valve	Landvélar	629000/266	N/A	1
Flow valve	Landvélar	088500002	N/A	1

Table 2.1: Bill of materials for the supplied structural parts [14] [15]
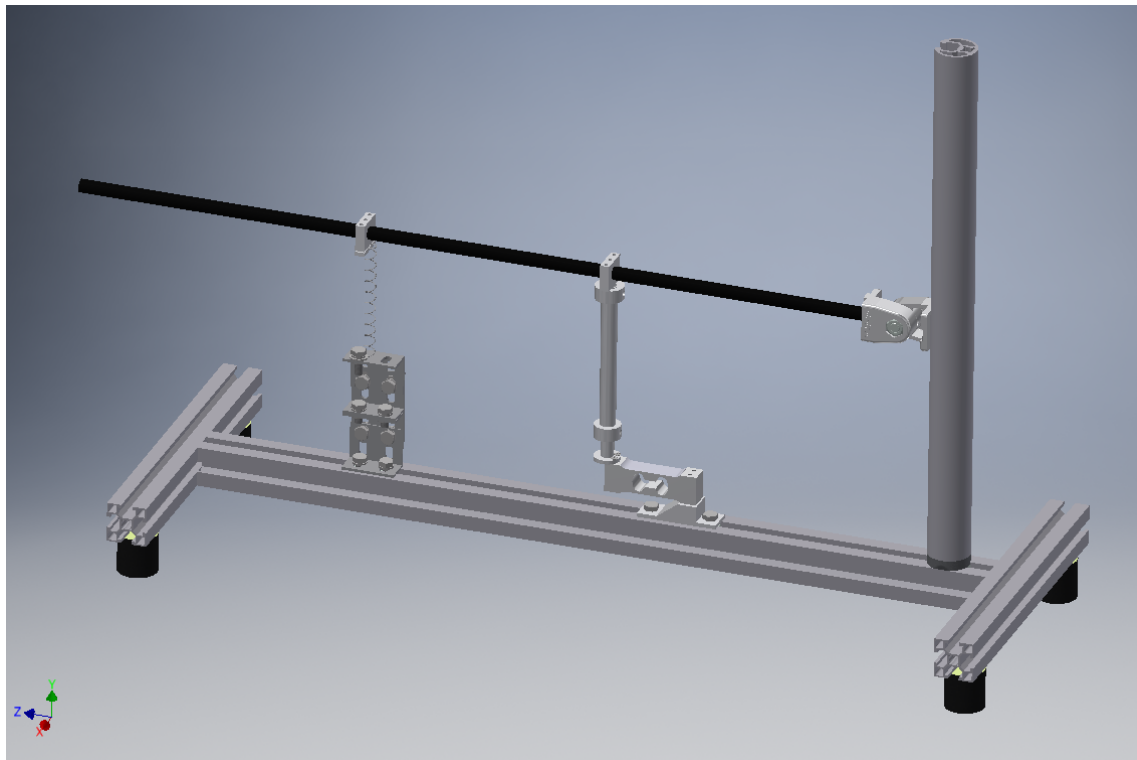
Figure 2.7: Final design 1

However, that solution would only supply a 10-bit integer for measurements, so to keep operation simple it was decided to use a LabView graphical programming interface. This interface is used to obtain data as well as control the current actuation and cooling system.

2.3.1 LabView

LabView System Design Software uses a graphical programming syntax in a manner to visualize, code and create engineering systems. The software simulates a control panel that gives
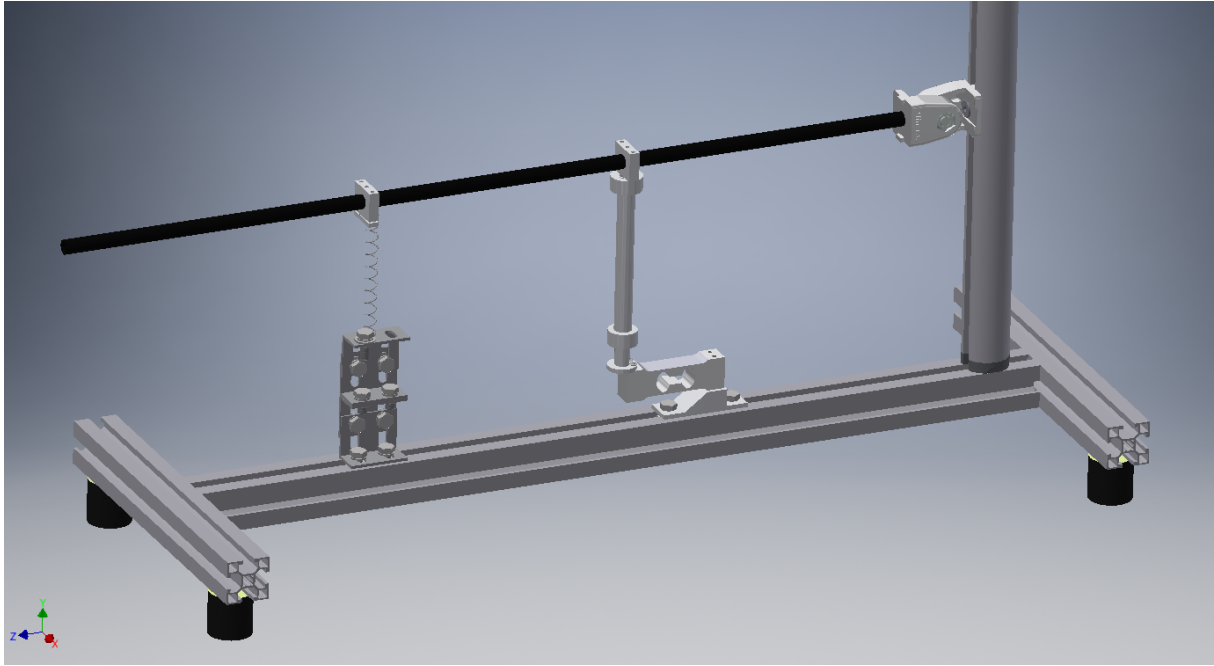
Figure 2.8: Final design
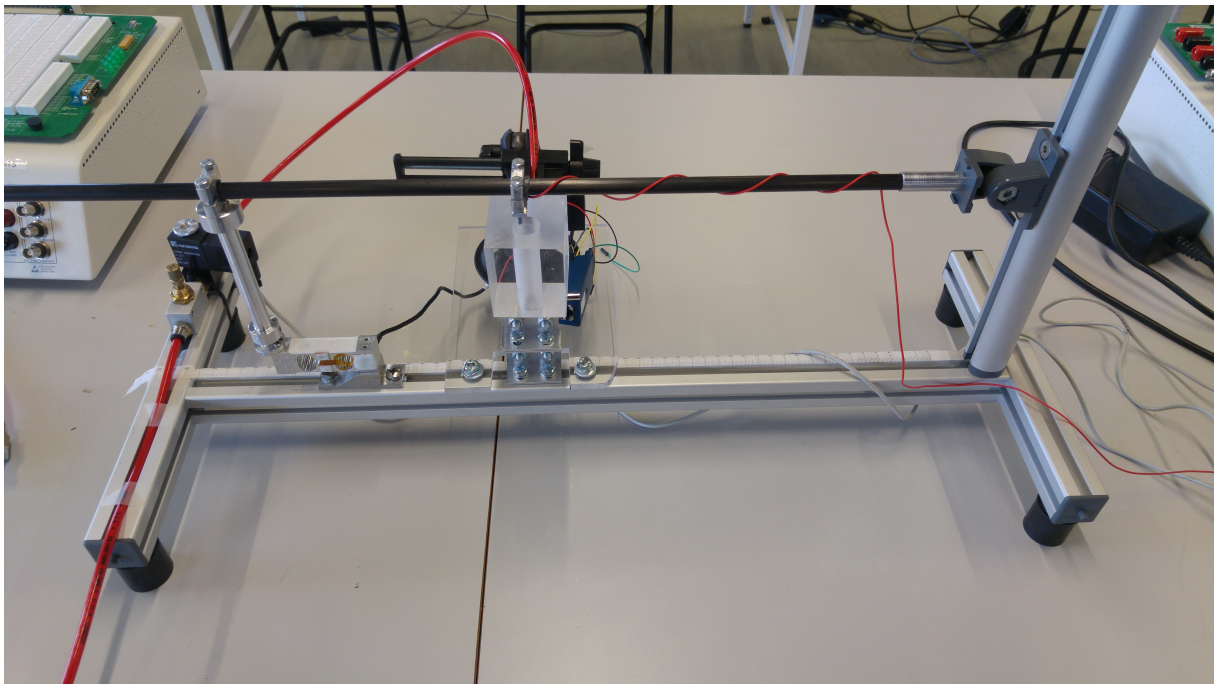
Figure 2.9: Completed build of testing frame. Detailed schematics in Appendix B.

the user a good overview of the current DAQ while simultaneously gathering reliable data. It is owned by National Instruments (NI) that also provide DAQ modules to connect directly to the desktop computer.

The developmental environment implemented in this experiment can be broken down into three main parts; Data setup, DAQ control loop, and Relay control loop. All of these parts are centrally controlled via a simulated control panel.
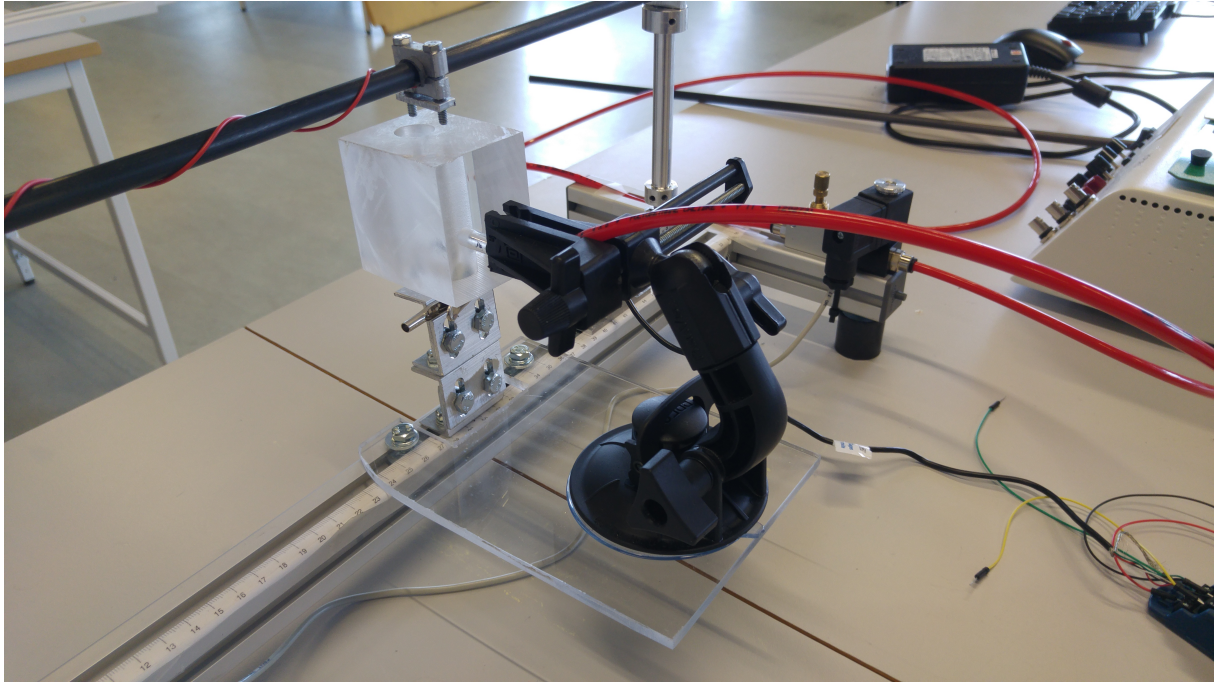
Figure 2.10: Closeup of the pneumatic cooling mount. Detailed schematics in Appendix B.

2.3.1.1   Data setup

Data setup runs as the program is initialized. The file directory is set, allowing the user to select an optional subfolder. The user inputs the file name as well as an optional message for the first line and the program creates that text file. Data setup defines the second line as Time, Force and Current since those are the variables that will be saved by the main DAQ loop. The relevant graphical representation can be seen in Figure 2.11.
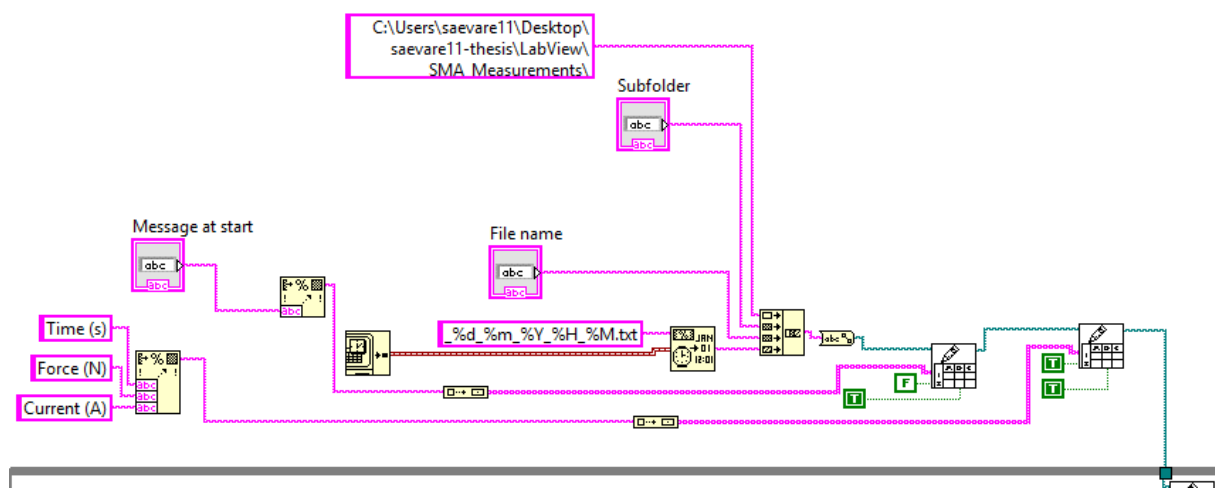
Figure 2.11: Interface for the data setup.

2.3.1.2   DAQ control loop

The main loop of the program is Data acquisition, or DAQ, and can be seen in Figure 2.12. When the program is initialized, it receives data for which text file directory to write to, the

current time (to subtract from in each loop), and the USB devices for the load cell and the shunt.

In each loop, the DAQ control performs the following tasks:

1. Takes a value from the load cell and displays it in mass directly on the load cell, mass measured from the spring (after set scaling) and in a plot as raw force data.

2. Gets a voltage drop value from the shunt resistance, offsets it and calculates the current measurements.

3. Takes the time counted since the current loop started by withdrawing the current time in seconds from the one acquired when the loop started.

4. Finally it returns those three data points to the text file.

Personalized user settings will be explained in the main control section.

Figure 2.12: DAQ control loop

2.3.1.3   Relay control

The relay control, Figure 2.13, consist of a timed loop that activates on a set interval and switches the two variables, actuation, and cooling. In addition, it holds a feedback loop that counts the number of iterations in the current experiment.

Figure 2.13: Relay control loop

2.3.1.4   Control panel

The control panel, Figure 2.14, is a simulated physical panel with buttons, gauges and text inputs that give the user full control over the interface. Prior to starting the experiment, the user selects the following features:

1. Optional message at the start, for the first line of data.

2. Optional sub-folder for the data. Must be an existing folder and end with a "\".

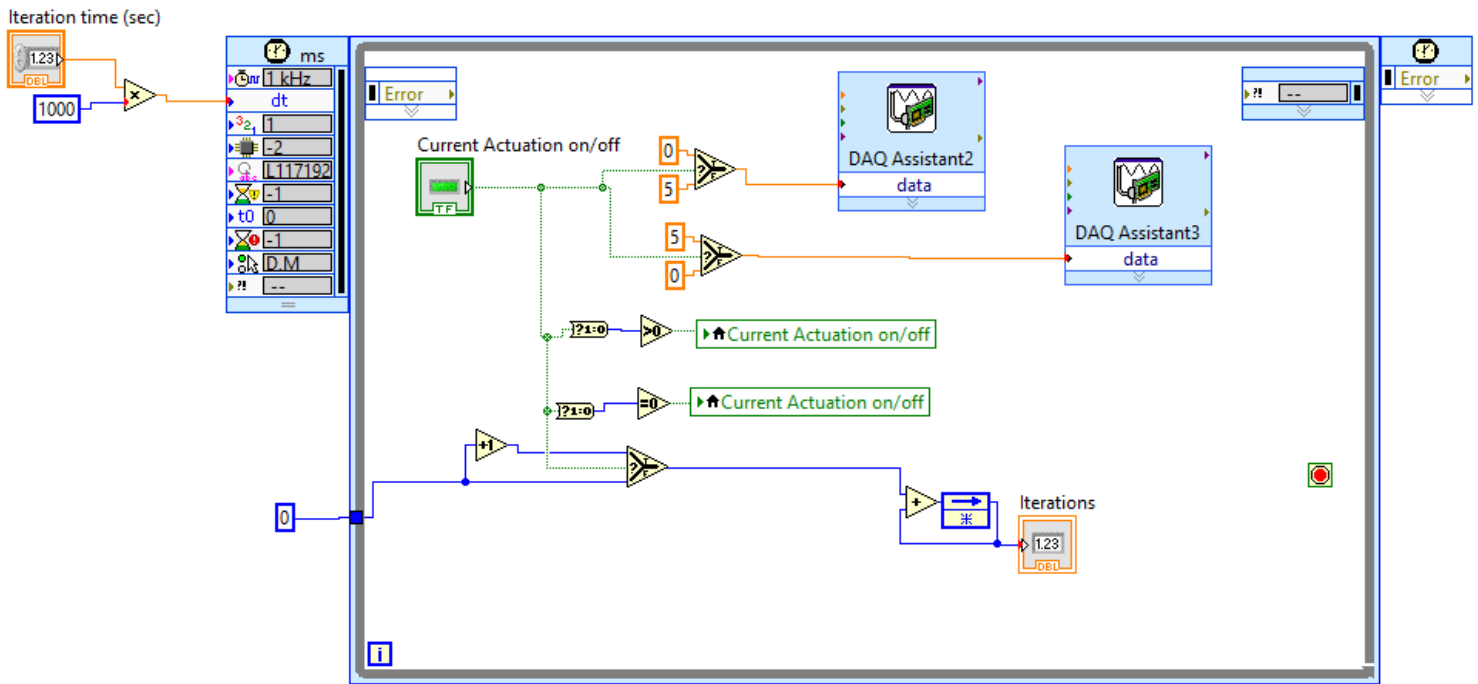3. File name, adds to the current date, which is the default file name in the following format: "Filename_DD_MM_YYYY_HH_MM.txt"

4. DAQ frequency, normally 10 in this experiment to give a decent data curve without unnecessarily large datasets, thereby following axiom 2 [11].

5. Load cell device, different for each USB input.

   Offset before multiplier - if the user needs to offset raw strain from the load cell.

   Load cell multiplier - calculated for a specific load cell during calibration (see Section 3.1).

   Offset after multiplier - similar to a "tare" button on a conventional weighing scale. Used to nullify or shift the force value measured if needed.

   Load cell distance - measured from the point about which the lever arm works to the load cell arm.

   Spring distance - measured from the point about which the lever arm works to the SMA spring itself.
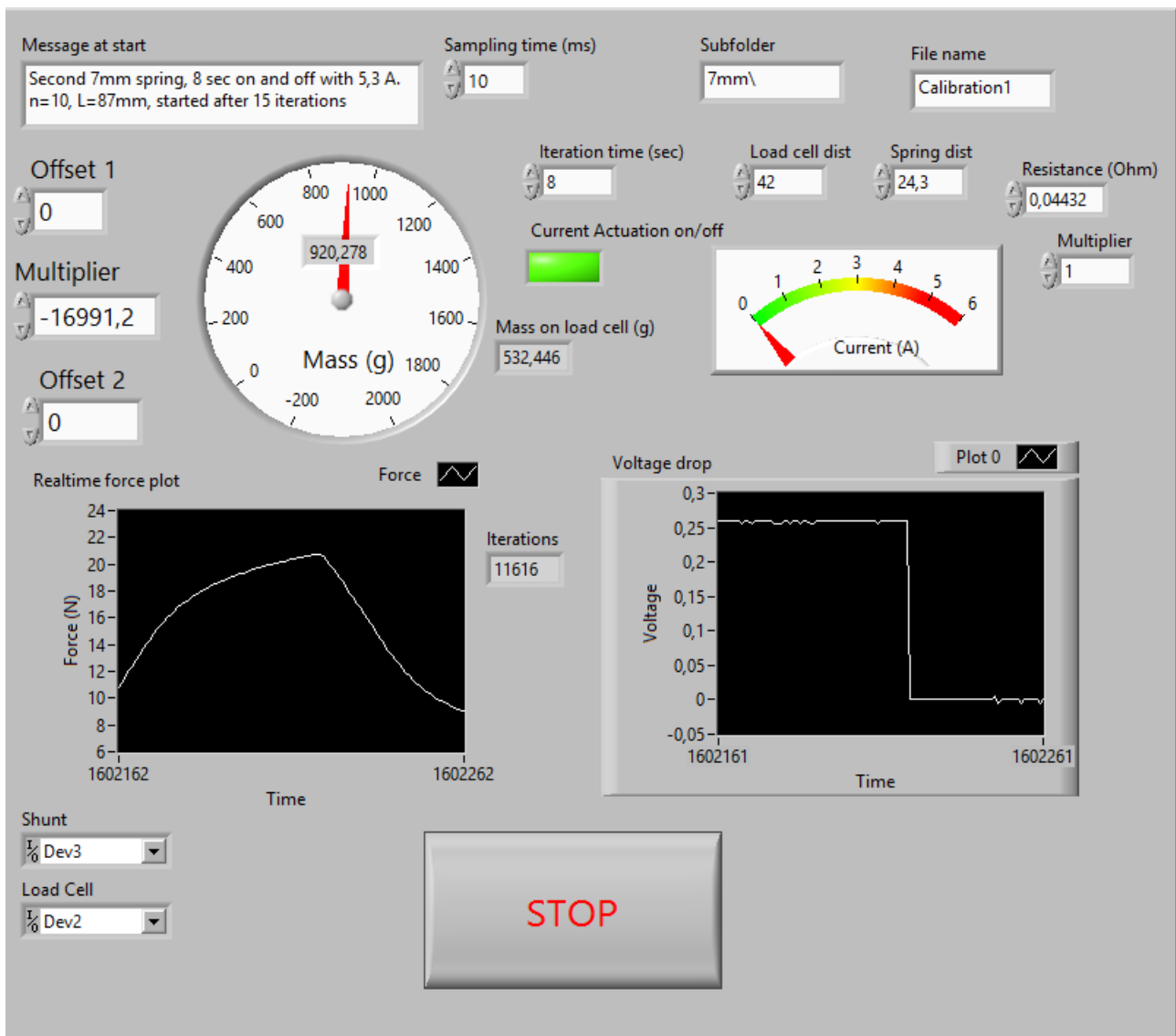
6. Shunt device, different for each USB input.

Figure 2.14: Main control panel of the DAQ program

Shunt multiplier - to scale the voltage drop over the shunt resistance if needed (-1 in this case).

Restistance - of the shunt being used.

7. Iteration time to wait between switching the relays from actuation to cooling and vice versa.

2.3.2   Circuit Design

In this experiment, it is necessary to keep the design as simple as possible, while still gathering essential data. Initially, it was designed to switch the relays with only the current from the analog switch connected to the desktop computer, but that current proved insufficient; P-channel power MOSFET was added to each relay circuit. Since the switch voltage is greater than the MOSFET is rated for, resistors 1 & 3 are added for compatibility. For security, resistors 2 & 4 are used as pull down resistors to help pull the TTL output voltage down to 0V when the MOSFET is switched off (Figure **??**). [16]

Reference	Name	Manufacturer	Part number	Qty.	Description
D1, D2	Zener			2	Flywheel Diode
R1, R3	Resistor			2	1 kΩ resistor
R2, R4	Resistor			2	10 kΩ resistor
R5	Shunt resistor	Holloway	Type SW	1	0,05 Ω Shunt resistor
RY1, RY2	Relay	Schrack	RT315005	2	5VDC, 16A/250VAC
Q1, Q2	R03W	Intl. Rectifier	IRFD911O	2	P-channel MOSFET
U1	Solenoid valve	Flo Control	629000/266	1	Cooling system switch
U2	SMA Spring		SMA Spring	1	Spring to be tested

Table 2.2: Bill of Materials for the circuit.

In addition, a shunt resistance is implemented to measure current. The voltage drop is measured over the known resistance of $R = 0,05$ Ω (Table 2.2) and the resultant electrical current calculated via Equation 2.8.
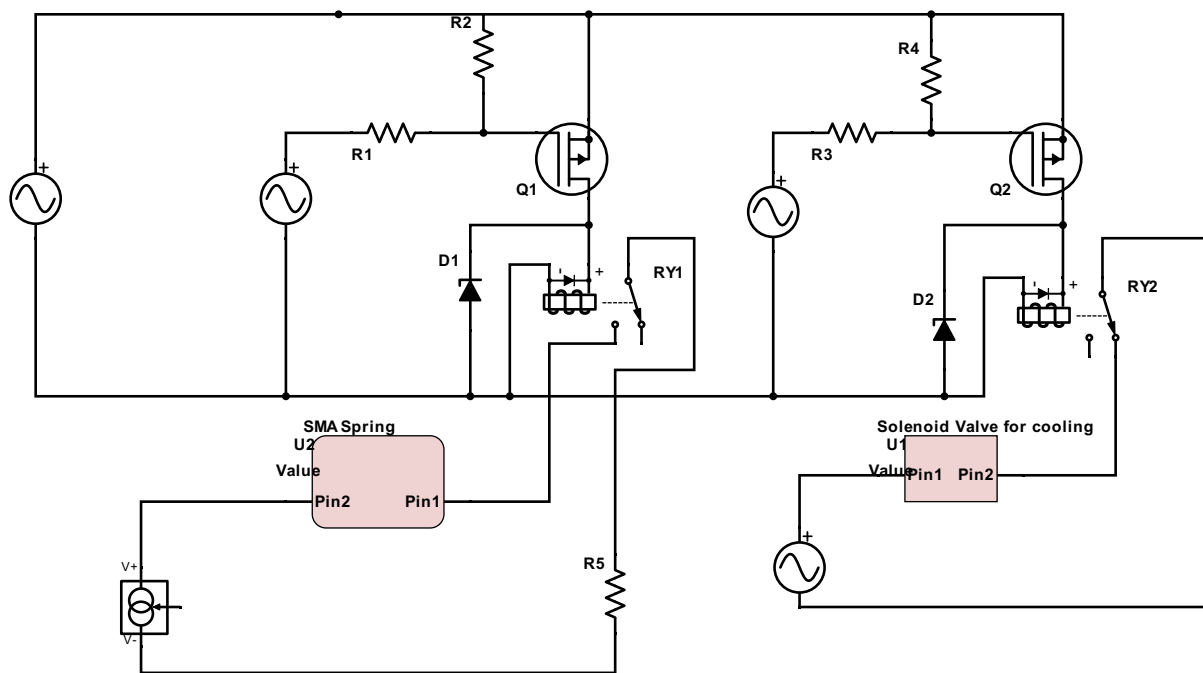
$$I = \frac{V}{R} \tag{2.8}$$

Figure 2.15: Completed circuit with two relays and power MOSFETs BOM in Table 2.2

2.4 Cost analysis

With an initial budget of 50.000 ISK, the total cost for all supplied materials can be seen in Table 2.3.

Item	Supplier	Cost	Currency	Cost (ISK)
Collection of extrusions and frame fasteners	MiniTec	202,3	EUR	26.855
Pultruded carbon tube	Goodwinds LLC	79,78	USD	9.357
Relays and connectors	Íhlutir	2.621	ISK	2.621
Pneumatic valves and connectors	Landvélar	8.621	ISK	8.621
Various bolts and fasteners	Byko	1.900	ISK	1.900
Total				49.354

Table 2.3: Suppliers bill of materials for cost analysis. Details in appendix.

Chapter 3

Results

With the setup ready and LabView running properly, the test rack delivered 6 complete datasets (sets of 10.000 actuations without interruptions), performed from 26.07.2016 to 16.08.2016.

3.1 Preliminary Calculations

While the setup was ready for gathering data, a few key elements required assessment.

3.1.1 Load Cell Multiplier

In essence, the load cell in question consists of two strain gauges, delivering varying resistance values because of their equal and opposing strain. The actual force values portrayed in this chapter are derived from the strain being measured by the National Instruments DAQ module and multiplied by a pre-calculated factor, in this case -16991,2. The load cell is calibrated by placing a known weight (w) onto it. It will return measurements for raw strain in the sensor (s) that is directly proportional to the force measurements required, so the necessary factor (f) can be found with:

$$f = \frac{w}{s} \tag{3.1}$$

Before starting each set of measurements, the test frame was calibrated by tuning the values for load cell dist. & spring dist. (section 2.3.1.4). Initially, a measured value from the hinge point was entered to the simulated control panel. As this is a pure ratio that LabView uses to scale the measurements, the calibration procedure was to place weights on top of the spring mount and confirm the measured force. Each dataset was calibrated to within 1% range of correct values for both 200g and a 400g weight.

3.1.2 Spring Choice

Multiple spring diameters and lengths were explored with the available wire diameters (0,1905 mm and 0,8128 mm). For easily scaled measurements, the goal was to use a spring with as high of a force as possible. The possible force range with that range of wire would be $0, 49 - 24$N, equivalent to a mass of $0, 05 - 2, 45$kg. As the objective was to get the highest range possible, so the heaviest spring was desired for the final measurements. Therefore, it was decided to run a set of tests with a 7mm inner diameter spring and 10 revolutions.

Manufacturer:	Confluent Medical Technologies / ndc
Web P/N:	WSM003200000DE
Production date:	27.2.2015
Form:	Wire
Function:	Shape Memory
Diameter:	0,8128 mm (0,032")
Type:	As-Drawn
Surface finish:	Chemically Pickled
Quantity:	9,144m (30 ft.)
NDC L/N:	4434

Table 3.1: Properties of NiTi wire used in measurements.

3.1.3   Resistive Heating

The level of resistive heating is of concern in order to determine the magnitude of current to supply to the spring without overheating it. In order to acquire rapid actuation but still prevent overheating, preliminary testing was performed and a current of $I = 5,3\mathrm{A}$ was chosen. With that level of current, an actuation cycle of 8 seconds on and 8 seconds off supplied the cycles for the results presented.

3.2   Data Collection

To ensure statistical significance in the results, the test was repeated six times with the same type of spring and the same elongation of the spring (86mm). Detailed wire properties are listed in Table 3.1.

Following the procedures described in section 2.1.1, all were cut from the same (longer) spring and only actuated with the DAQ running. In addition, all received 5,3 A of actuation current. Each complete dataset ran for at least 10.000 cycles.

3.2.1   Test Run

While the first spring was being tested, LabView had some problems with the connections to the DAQ module. The load cell DAQ stopped working momentarily, resulting in the DAQ restarting itself and requiring the user to intervene by pressing "Continue" on screen. Before that intervention, the relay control loop continued its cycle. This occurred twice during the first cycle, resulting in a loss of data as can be seen in Figure 3.3. Therefore, this cycle is labeled a test run. The cause was found to be rather unstable connections to the shunt resistance as well as the DAQ module. These issues were addressed and a similar loss of data did not occur again.

Although this set is incomplete, a certain trend may still be noted in the maximum values over iterations as can be seen in Figure 3.3 which is certainly promising for the next sets of data.

Finally, the spring broke after 6.956 iterations. Detailed snapshot from a digital microscope can be seen in Figure 3.2

3.2.2   Dataset 1

The second spring test ran without incident. Testing an identical spring, there were no interruptions in the DAQ or failure of the spring. This test ran for 11,600 iterations at $5,3\mathrm{A}$ actuation current and the data showed a definitive trend in the development of average force values, as

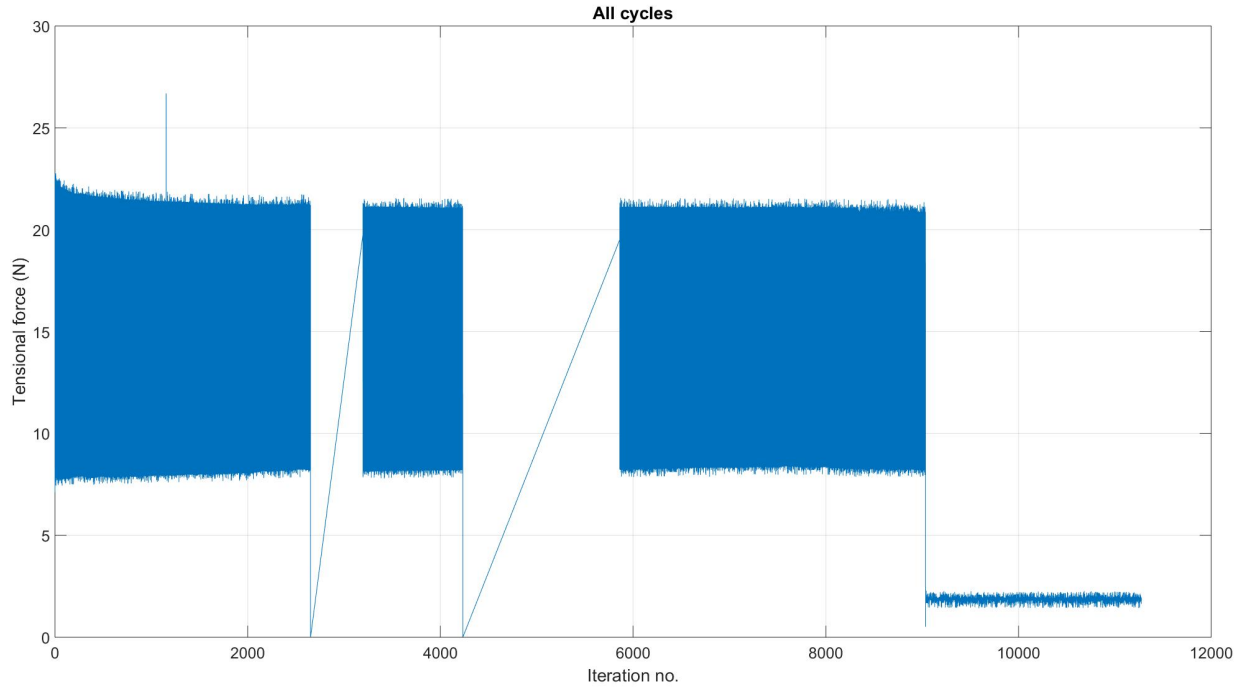Figure 3.1: Overview of all cycles from the first spring

(a)   (b)   (c)
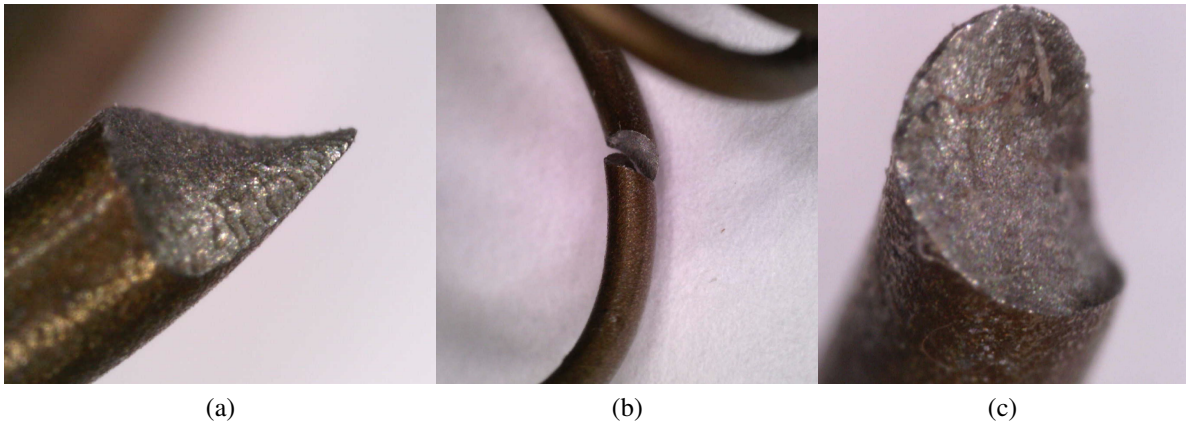
Figure 3.2: Close up images of the fractured first spring. This was the only fracture that occurred.

seen in Figure 3.5. This spring followed a trend for the first 1.500 or so iterations, showing initial degradation of 2,65%.

The resultant data delivered a maximum force of $21,95$N and shows a definitive exponential decay curve with the following curve fit equation (Other curve fit constants in section 3.3):

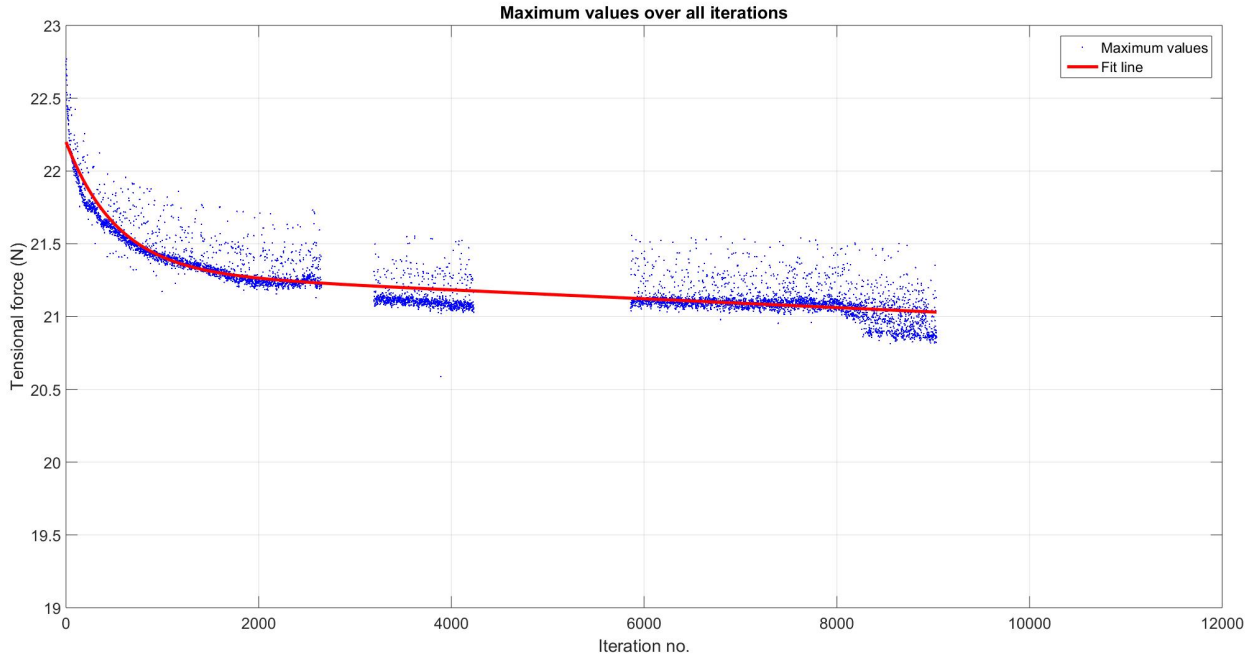$$f(x)_1 = 0,8044e^{-0,00096x} + 21,25e^{-1,88e-6} \tag{3.2}$$

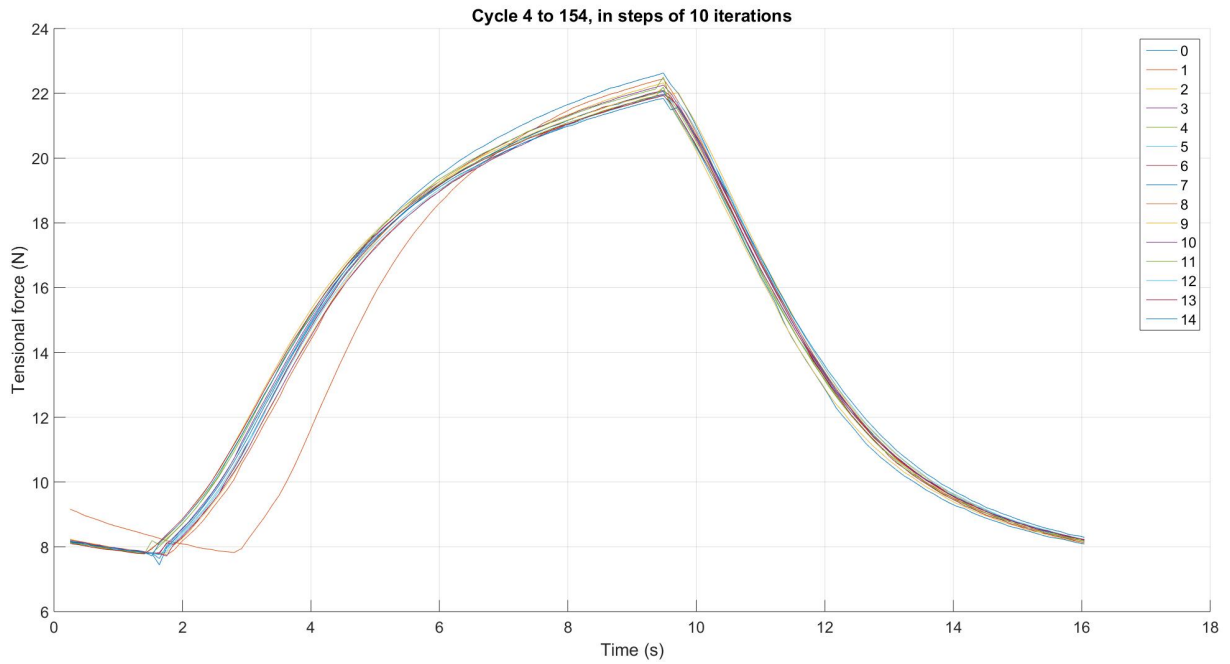Figure 3.3: Maximum values of test spring over 6.956 iterations

Figure 3.4: Test spring; whole actuation cycles 1-151 in steps of 10

3.2.3   Dataset 2

The second complete dataset delivered 11.977 iterations of 5,3 A actuation current. The resultant data delivered a maximum force of $22,11\mathrm{N}$ and shows a definitive exponential decay curve with the following curve fit equation (Other curve fit constants in section 3.3):
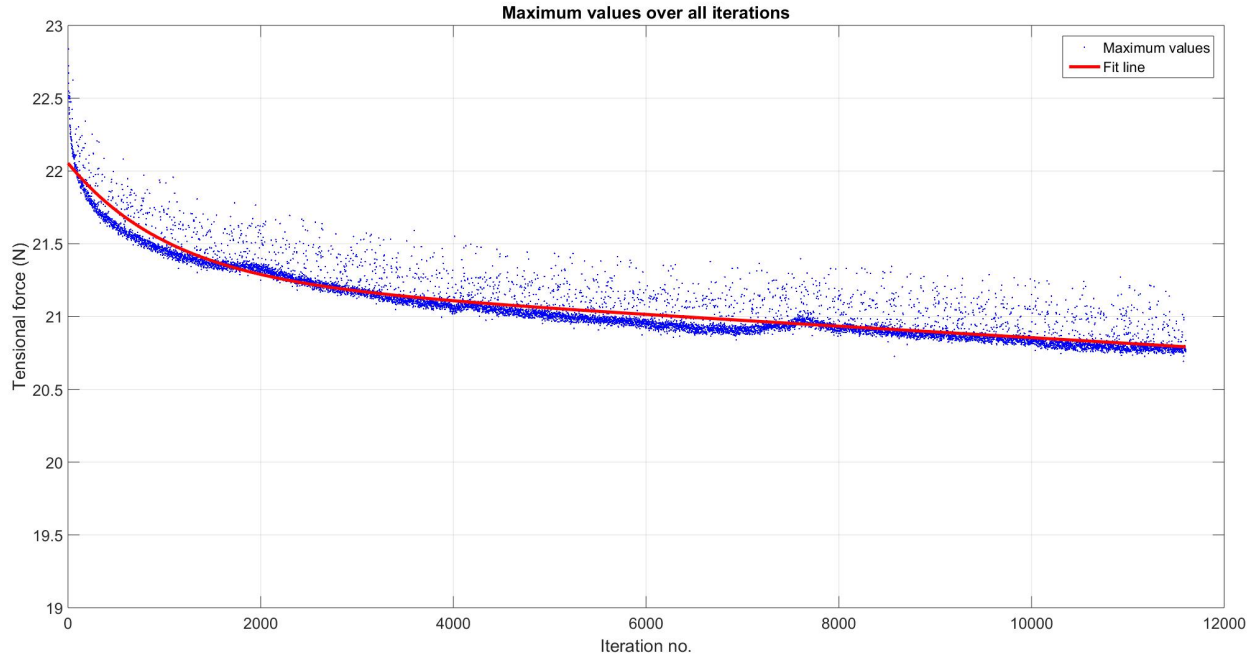
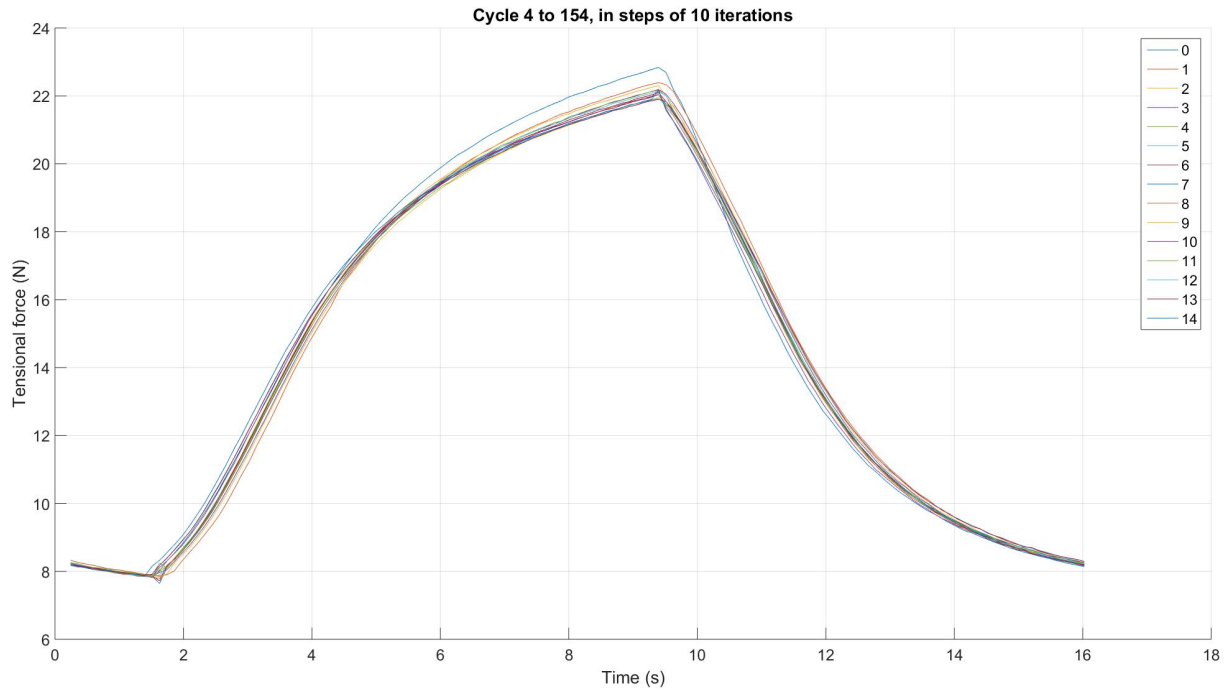Figure 3.5: Maximum values of first spring over 11.600 iterations

Figure 3.6: First spring; whole actuation cycles with 10 iterations between.

$$f(x)_2 = 0,8094e^{-0,00116x} + 21,47e^{-2,36e-6} \tag{3.3}$$
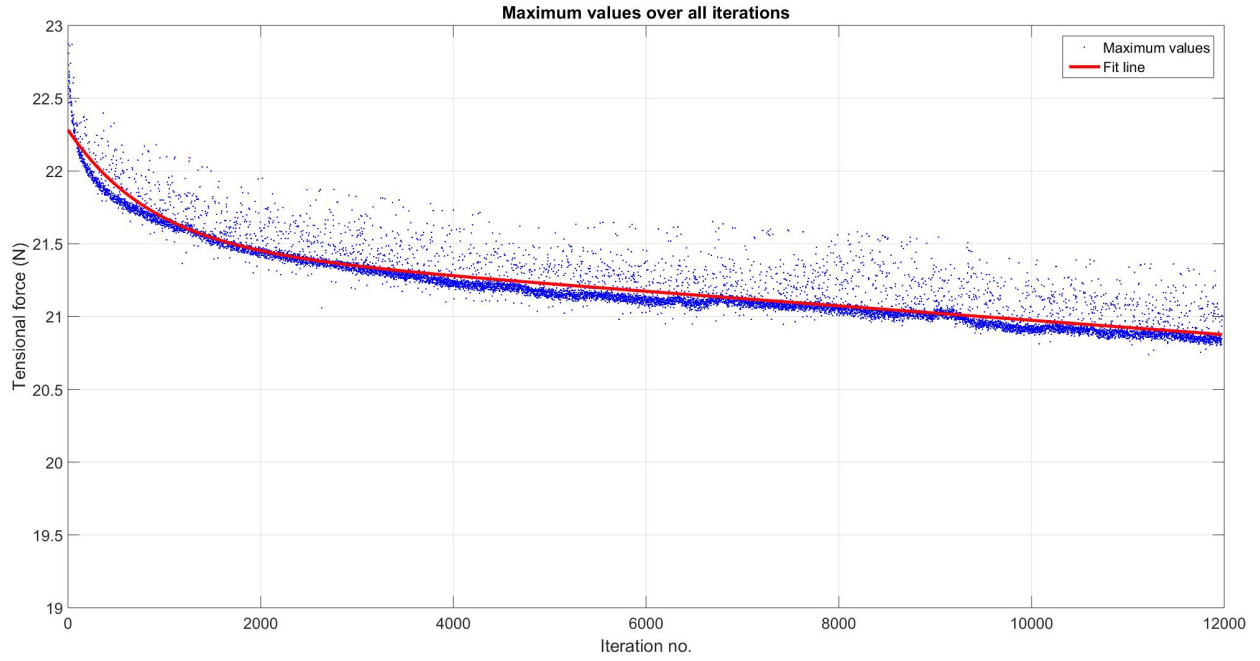
Figure 3.7: Maximum values of second spring over 11.977 iterations
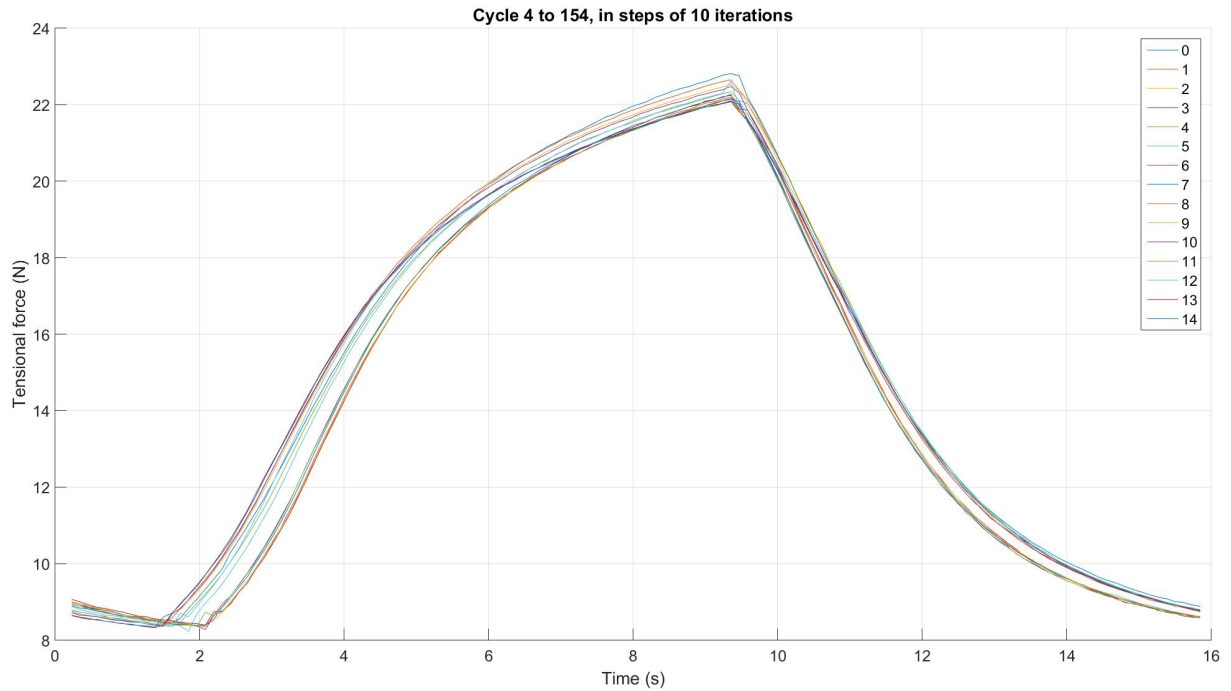
Figure 3.8: Second spring; whole actuation cycles with 10 iterations between.

3.2.4   Dataset 3

The third complete dataset delivered 11.102 iterations of 5,3 A actuation current. The resultant data delivered a maximum force of 21, 76N and shows a definitive exponential decay curve with the following curve fit equation (Other curve fit constants in section 3.3):

$$f(x)_3 = 0,9665e^{-0,00195x} + 21,08e^{-2,83e-6} \qquad (3.4)$$

Figure 3.9: Maximum values of third spring over 11.102 iterations

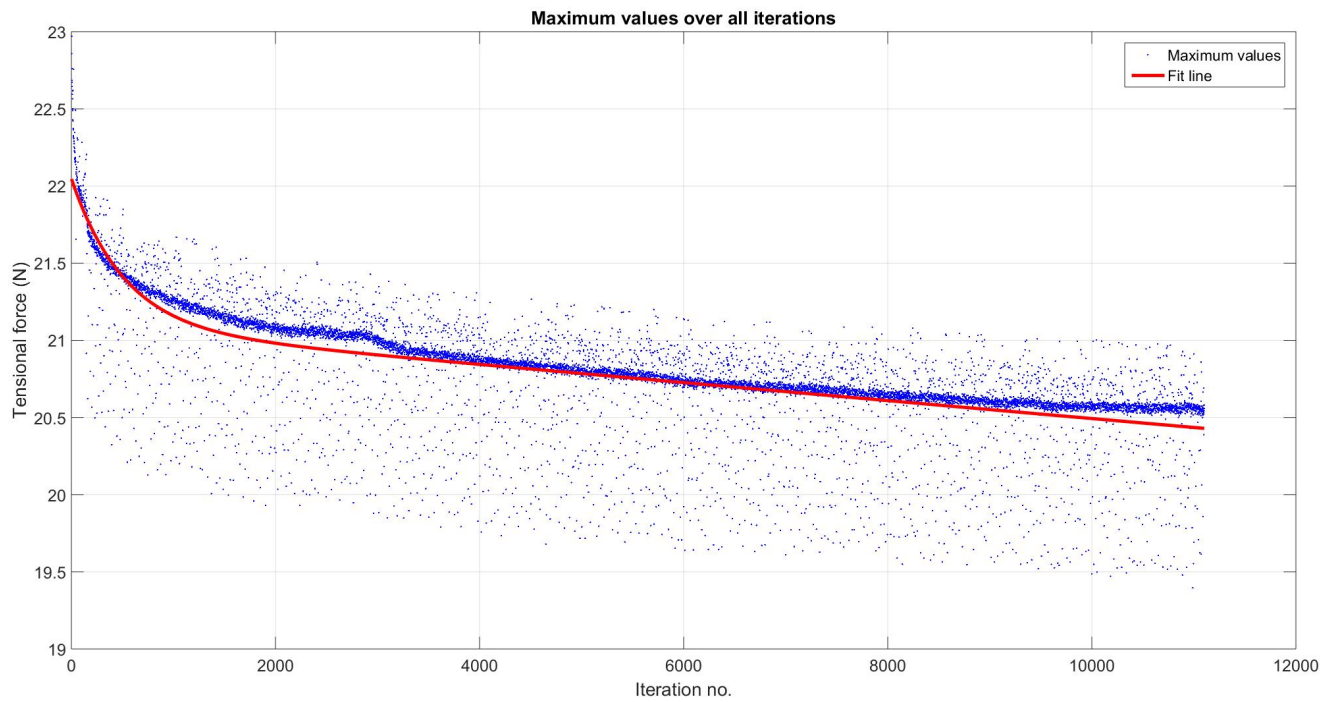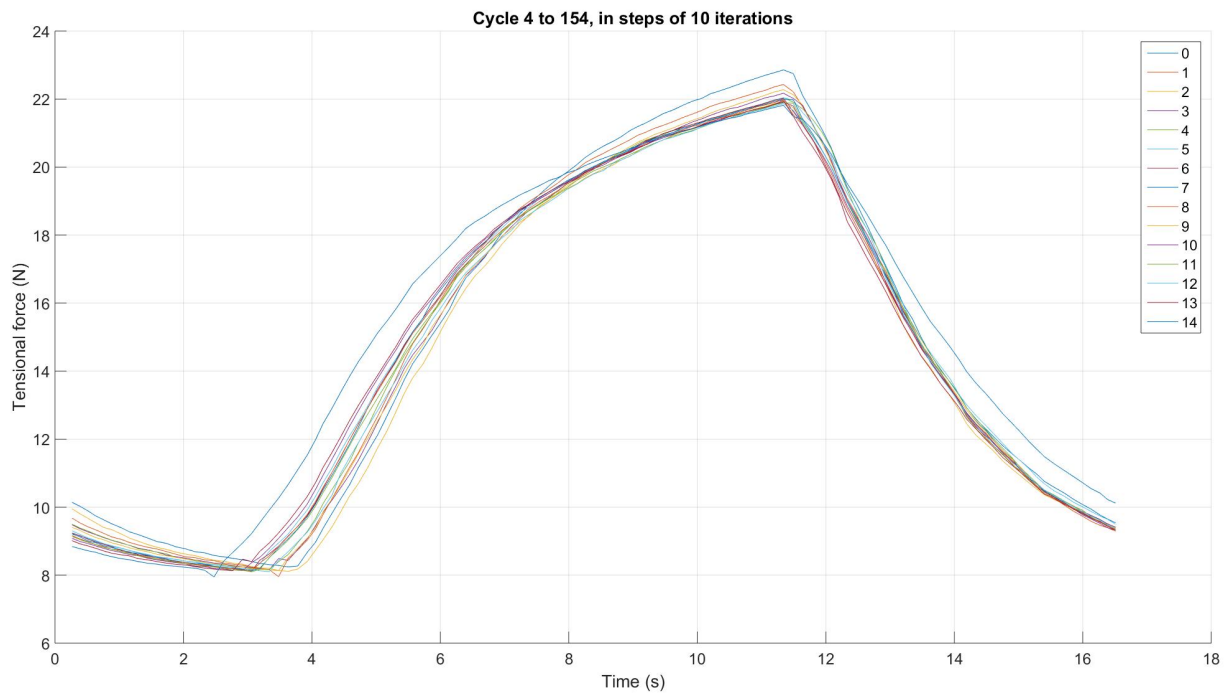Figure 3.10: Third spring; whole actuation cycles 1-151 in steps of 10

3.2.5 Dataset 4

The fourth complete dataset delivered 11.779 iterations of 5,3 A actuation current. The resultant data delivered a maximum force of $20, 84$N and shows a definitive exponential decay curve with the following curve fit equation (Other curve fit constants in section 3.3):

$$f(x)_4 = 0,8749e^{-0,00135x} + 20,20e^{-2,89e-6} \tag{3.5}$$
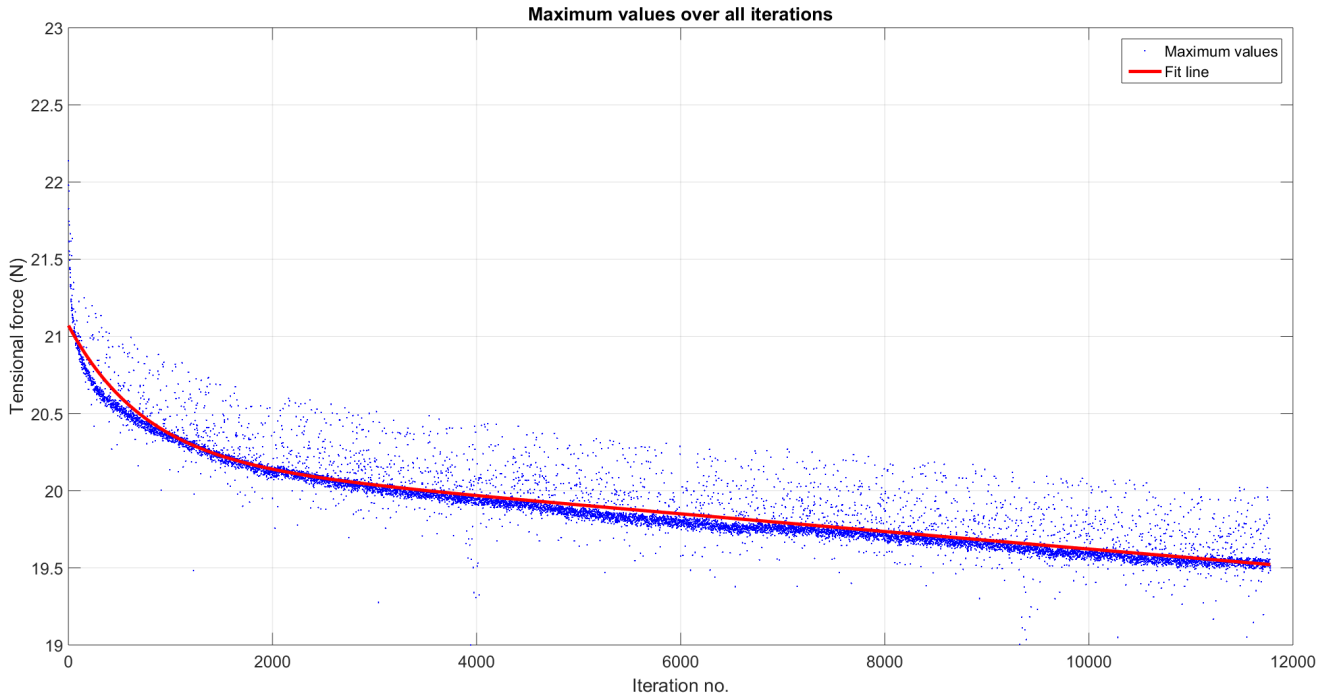
Figure 3.11: Maximum values of fourth spring over 11.779 iterations

3.2.6 Dataset 5

The fifth complete dataset delivered 10.102 iterations of 5,3 A actuation current. The resultant data delivered a maximum force of $20, 93$N and shows a definitive exponential decay curve with the following curve fit equation (Other curve fit constants in section 3.3):

$$f(x)_5 = 1,035e^{-0,00216x} + 20,24e^{-2,49e-6} \tag{3.6}$$

3.2.7 Dataset 6

The sixth complete dataset delivered 10.211 iterations of 5,3 A actuation current. The resultant data delivered a maximum force of $19, 91$N and shows a definitive exponential decay curve with the following curve fit equation (Other curve fit constants in section 3.3):

$$f(x)_6 = 0,001595e^{-3,465x} + 19,24e^{-0,0047} \tag{3.7}$$

Figure 3.12: Fourth spring; whole actuation cycles 1-151 in steps of 10
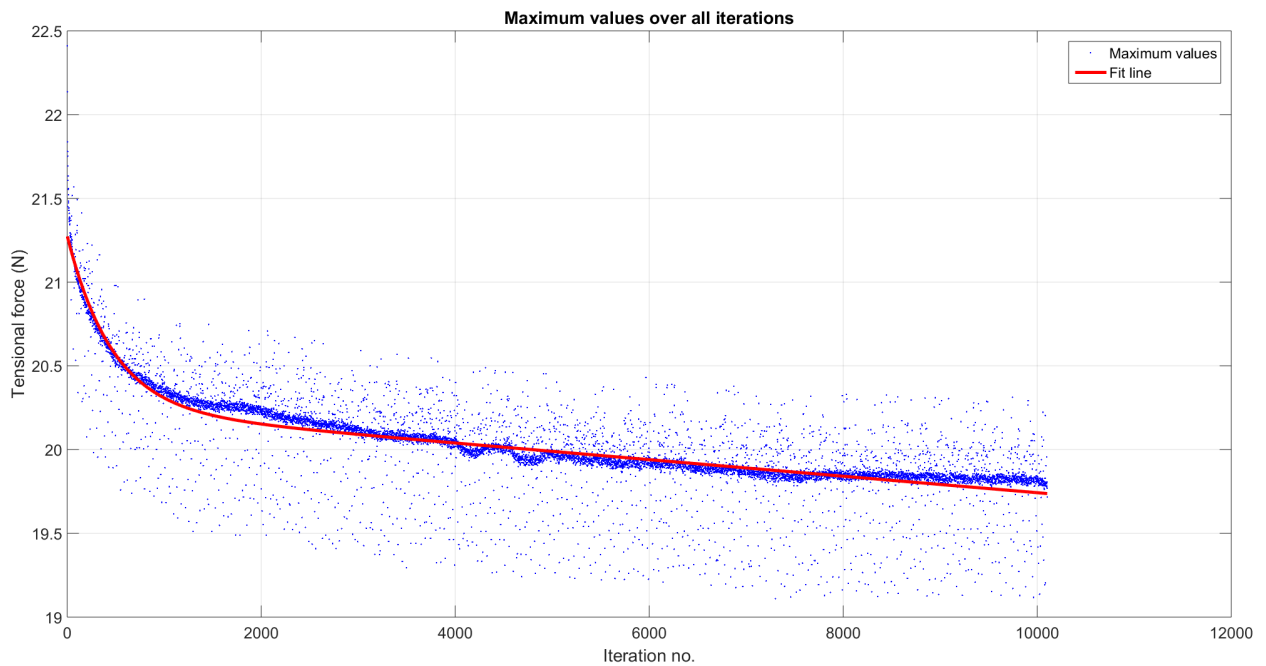
Figure 3.13: Maximum values of fifth spring over 10.102 iterations

3.3 Data summary

Observing the data as a whole, the actuation force can be expected to follow an exponential decay as a function of cycles actuated. An average degradation of 2,41% can be expected for the first 1.500 iterations, an additional 0,68% for the next and so on as can be seen in Table

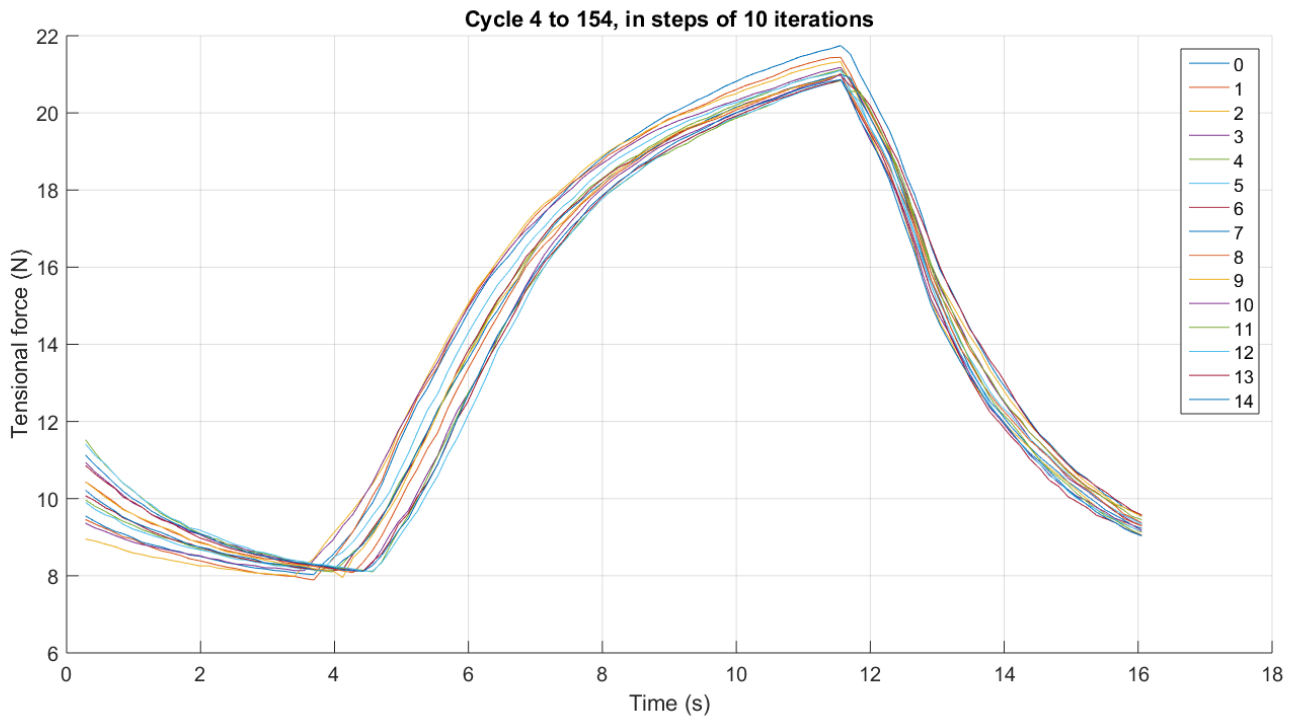Figure 3.14: Fifth spring; whole actuation cycles 1-151 in steps of 10

Figure 3.15: Maximum values of sixth spring over 10.211 iterations

3.2. The average degradation is calculated as the mean of all data recorded in steps of 1.500 iterations.

Figure 3.16: Sixth spring; whole actuation cycles 1-151 in steps of 10

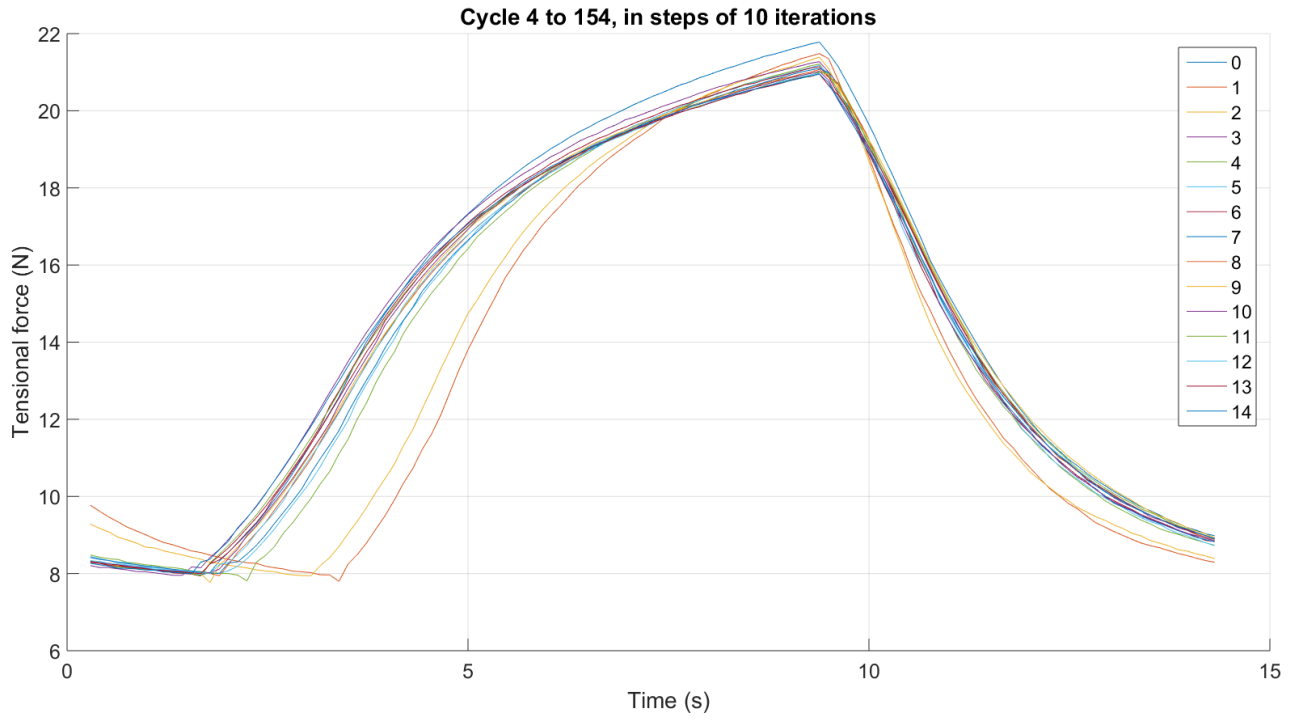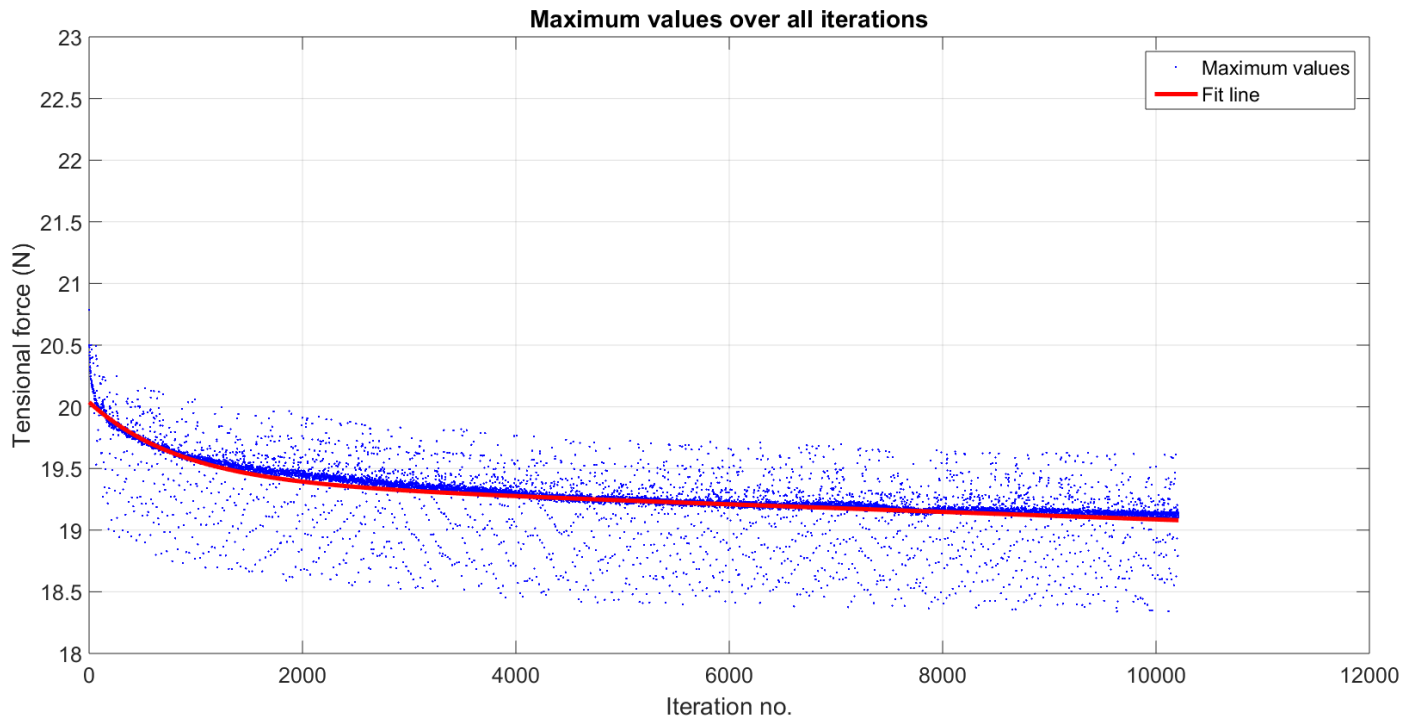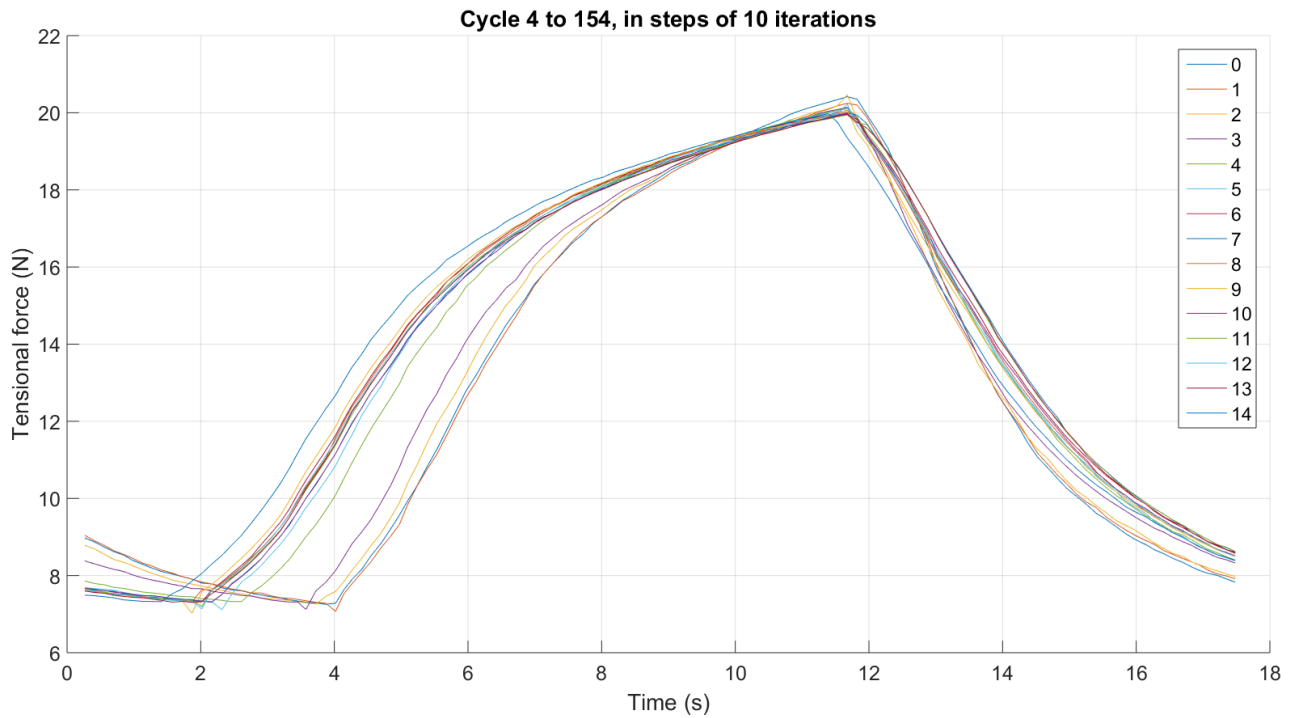| Iteration no.	100	1.500	3.000	4.500	6.000	7.500	9.000	10.500
Data 1 Force (N)	21,95	21,37	21,21	21,06	20,97	20,98	20,91	20,84
Data 2 Force (N)	22,11	21,55	21,38	21,22	21,13	21,11	21,06	20,94
Data 3 Force (N)	21,76	21,08	20,93	20,77	20,69	20,63	20,53	20,51
Data 4 Force (N)	20,84	20,24	20,04	19,95	19,80	19,78	19,69	19,59
Data 5 Force (N)	20,93	20,25	20,10	20,00	19,91	19,82	19,82	
Data 6 Force (N)	19,91	19,47	19,34	19,23	19,19	19,15	19,12	
Average Force (N)	21,25	20,66	20,50	20,37	20,28	20,24	20,19	20,47
St. dev. (Force)	0,77	0,73	0,73	0,70	0,70	0,71	0,70	0,53

Table 3.2: Force data averages with spacing of 1.500 iterations.

Iteration no.	1.500	3.000	4.500	6.000	7.500	9.000	10.500
Dataset 1	-2,65%	-3,44%	-4,14%	-4,55%	-4,51%	-4,85%	-5,17%
Dataset 2	-2,60%	-3,37%	-4,11%	-4,56%	-4,67%	-4,89%	-5,47%
Dataset 3	-3,18%	-3,89%	-4,64%	-5,07%	-5,36%	-5,82%	-5,95%
Dataset 4	-2,93%	-3,96%	-4,37%	-5,15%	-5,27%	-5,71%	-6,23%
Dataset 5	-3,29%	-4,06%	-4,54%	-5,03%	-5,46%	-5,43%	
Dataset 6	-2,20%	-2,87%	-3,45%	-3,65%	-3,87%	-4,04%	
Average	-2,81%	-3,60%	-4,21%	-4,67%	-4,85%	-5,12%	-5,71%
St. Dev.	0,37%	0,42%	0,39%	0,51%	0,56%	0,61%	0,41%

Table 3.3: Degradation data

A curve fit was performed in Matlab for all datasets, with all factors describing the relevant regression statistics listed in Table 3.4. The coefficients listed are are unique constants for each variable in the following curve fit equation:

Coefficients	data1	data2	data3	data4	data5	data6
a	0,8044	0,8094	0,9665	0,8749	1,035	0,001595
b	-0,00096	-0,00116	-0,00195	-0,00135	-0,00216	-3,465
c	21,25	21,47	21,08	20,2	20,24	19,24
d	-1,88E-06	-2,36E-06	-2,83E-06	-2,89E-06	-2,49E-06	-0,0047
Goodness of fit						
SSE	95,35	117,1	704,4	150,6	276,7	364,3
R^2	0,893	0,8909	0,5617	0,8776	0,7029	0,5065
RMSE	0,09068	0,0989	0,2519	0,1131	0,1655	0,1889

Table 3.4: Factors and coefficients describing data curve fits.

$$f(x)_1 = ae^{bx} + ce^d \tag{3.8}$$

One measure of how closely the curves follow the empirical data is the goodness-of-fit test [17]. It consists of three main values for each fit:

The sum of squares due to error (SSE): A value describing the total deviation of the measured values from the fitted curve. A lower value indicates a more useful fit for prediction, or smaller random error components.

R-squared: A coefficient with a value between 0 and 1 representing how successful the fit is in predicting actual values. Higher values indicate that a greater proportion of variance is accounted for by the fitted curve.

Root mean squared error (RMSE): This is an estimate of the standard deviation of the random component in the data. A lower value indicates a more useful fit.

Chapter 4

Discussion

4.1 Summary

Employing Shape Memory Alloys in actuation has proven to be effective to acquire effective actuation without requiring a large net volume, multiple moving parts, or complicated assemblies. This is made possible by the Shape Memory Effect (SME) which is, in essence, a solid-solid reversible phase transformation between low-temperature martensite and high-temperature austenite. When heated, the alloy retains the previous shape, thereby inducing the SME useful for actuation.

The long-term cyclic degradation of the force exhibited during this SME has not previously been thoroughly examined to create a model for its development. Therefore, a testing rack has been designed and built to measure the degradation of NiTi springs when electrically actuated. The system was designed with significant scaling in mind to make it compatible with a large range of actuation forces. It was automated using LabView System Design Software for data acquisition and relay circuitry to switch between actuation and cooling.

This method produced six sets of data describing the force degradation of the springs in question. At least 10.000 actuations were performed, supplying 5,3A of current to each spring for 8 seconds on and off to generate data describing the development of the maximum forces involved. Each dataset showed a definitive curve of exponential decay with 5-6% maximum force degradation over 10.000 iterations.

4.2 Conclusion

Based on tests performed as part of this thesis, the degradation of SMA spring actuators follows a pattern of exponential decay, as stated in Table 3.4. We can expect $2,5\%$ degradation in the first 1.500, 3,2 % for the first 3.000, and approximately 0,5% more for each added 1.500 iterations. Prior to this experiment, a degradation of at least 20-30% and 40% fatigue break was expected by the author. However, the data shows considerably less degradation and shows a surprising level of reliability in the continual actuation from NiTi springs.

While the datasets were all individually consistent in terms of pure force degradation, there was a considerable drop in the overall force magnitude between springs measured. This may be due to an inconsistency in the individual setup of each spring test in terms of the exact placement of the springs on its fixture. Should the experiment be repeated, a more consistent mode of setup would have to be developed.

4.3   Future work

Certain modifications can be made to the setup to improve the data acquisition, including the following:

1. It is necessary to implement a more effective method of placing individual springs into the test rack to improve consistency in the magnitude of the measured forces.

2. A heat sensor could be added to the rack, perhaps fixed on the cooling system. As a thermocouple or thermistor would affect the spring temperature to some degree, an optical temperature sensor would be ideal to acquire temperature data.

3. For a further improved scaling of the forces involved, the carbon tube moment arm and/or the base profile could be lengthened.

4. A Monitoring system would be excellent to add to the LabView graphical interface. This would prevent further loss of data (as occurred in the test run) by perhaps notifying the user via email.

This research operates as a proof of concept for other possible studies, stating what can be expected from similar actuators in terms of degradation. The design and consecutive build of the moment arm test rack opens the door to continued research into the reliability of different types of SMA springs, as well as orthodontic muscle wire. To continue with this research, the following criteria should be explored:

1. Further testing of different wire gauges, spring diameters, and even alloys. A wide array of additional springs can be explored with the test rack since it employs a simple moment arm with a scalable force acting on the load cell. This would create quantifiable data and improve upon the current level of SMA spring design.

2. Similar testing could be done with an orthodontic muscle wire to see how elastic deformation compares with shape deformation.

Bibliography

[1] W. D. C. Jr. and D. G. Rethwisch, *Materials science and engineering*, B. Stenquist, Ed. Wiley, 2015.

[2] P. P. Jenkins and G. A. Landis, "A rotating arm using shape-memory alloy", *NASA*, 1995.

[3] D. C. Lagoudas, *Shape memory alloys- modeling and engineering applications*. Springer, 2008.

[4] L. Lecce and A. Concilio, *Shape memory alloy engineering*. Elsevier Ltd., 2015.

[5] R. Jorma. (Apr. 1999). Biocompatibility evaluation of nickel-titanium shape memory metal alloy. English, University of Oulu, Faculty of medi, [Online]. Available: `http://jultika.oulu.fi/Record/isbn951-42-5221-7`.

[6] J. R. S. Anadón, "Large force shape memory alloy linear actuator", M.Sc. Thesis, University of Florida, 2002.

[7] S. Kim, E. Hawkes, K. Cho, M. Jolda, J. Foley, and R. Wood, "Micro artificial muscle fiber using niti spring for soft robotics", *International Conference on Intelligent Robots and Systems*, 2009.

[8] Grand Illusions Ltd., Website, Aug. 2016. [Online]. Available: `http://www.grand-illusions.com/acatalog/Nitinol.html`.

[9] S. Degeratu, "On the design of a shape memory alloy spring actuator using thermal analysis", *WSEAS Transactions on Systems*, vol. 7, no. 1109-2777, pp. 1–2, Oct. 2008.

[10] W. Predki, M. Klönne, and A. Knopik, "Cyclic torsional loading of pseudoelastic niti shape memory alloys: Damping and fatigue failure", *Material Science and Engineering*, 2005.

[11] N. P. Suh, *The Principles of Design*. Oxford University Press, 1990.

[12] J. Guls, Ó. I. Bjarnason, Ó. Pétursson, S. Ö. Einarsson, and J. T. Foley, "Application of axiomatic design in desiging autonomous underwater photography lighting", *International Conference on Axiomatic Design*, 2016.

[13] VPG Transducers, "Aluminum single-point load cell", VPG Transducers, vpgt.americas@vpgsensors.com, Datasheet 12003, Dec. 2014.

[14] MiniTec GmbH & Co. KG. (Aug. 2016). Minitec profile systems. English. Profiles and fasteners, Minitec, [Online]. Available: `http://www.minitec.de/en//Web/produkte/Components/profile_system/Profile-sections.php`.

[15] Goodwinds LLC. (Jun. 2016). Pultruded carbon tubes. English, Goodwinds, [Online]. Available: `https://goodwinds.com/20978.html`.

[16] AspenCore Inc., *MOSFET as a switch*, website, Aug. 2016. [Online]. Available: `http://www.electronics-tutorials.ws/transistor/tran_7.html`.

[17] Matlab, *Evaluating goodness of fit*, Website, Aug. 2016. [Online]. Available: `http://www.mathworks.com/help/curvefit/evaluating-goodness-of-fit.html`.

Appendix A

Code

The data collected by LabView was processed by a Matlab program (`SMAplot.m`) that works in four parts:

1. Imports data into vectors and plots all time and force data in one plot for an overview.

2. Retrieves and plots whole data cycles with 10 iterations between.

3. Retrieves and plots whole data cycles with 500 iterations between.

4. Locates the maximum force measurements for each cycle and plots them together along with an exponential line fit.

Listing A.1: `SMAplot.m`: Data processing code for force measurements

```
1  function [x, export, n, stdev, goodness] = SMAplot( data2 )
   %UNTITLED Summary of this function goes here
3  % Detailed explanation goes here

5  T2 = data2(:,1);
   F2 = data2(:,2);
7  C2 = data2(:,3);

9  n = 1;
   s = true;
11 while s == true
       if T2(n)>1000
13         s = false;
       end
15     n = n + 1;
   end
17 n = 16*n./1000; %avg. number of data points in each cycle
   % for the first 1000 iterations
19
   %%
21
   %Plot entire set of data
23 figure(1)
   %plot(T2(1:floor(n*500)),F2(1:floor(n*500)))
```

```
25  plot(T2./16,F2)
    xlabel('Time (s)')
27  ylabel('Tensional force (N)', 'Fontsize', 15)
    grid on
29  title('All cycles', 'Fontsize', 15)
    xlabel('Iteration no.', 'Fontsize', 15)
31  ylabel('Tensional force (N)', 'Fontsize', 15)

33  %%

35  tempn = ceil(n); %Even number for index
    iter = 4; %First iteration to plot
37
    figure(2)
39  hold on
    for i = 1:1:15
41      tempF = F2((iter*tempn):((iter+1)*tempn)); %Values to plot
        [high(i), start] = max(tempF); %Find highest point to start plotting from for ←↩
                ↪consistency
43      start = start − 80; %Start a little bit earlier than the minimum datapoint
        tempF = F2((iter*tempn)+start:((iter+1)*tempn)+start); %Update values to plot
45      low(i) = min(tempF);
        plot(T2(3:(tempn+3)),tempF)
47      iter = iter + 10;
    end
49
    stdev(1) = std(low);
51  stdev(2) = std(high);

53  legend('0' , '1' , '2' , '3' , '4' , '5' , '6' , '7' , '8', '9', '10', '11', '12', '13', '14')
    grid on
55  title('Cycle 4 to 154, in steps of 10 iterations', 'Fontsize', 15)
    xlabel('Time (s)', 'Fontsize', 15)
57  ylabel('Tensional force (N)', 'Fontsize', 15)
    hold off
59
    %%
61  tempn = ceil(n); %Even number for index
    iter = 4; %First iteration to plot
63
    figure(3)
65  hold on
    for i = 1:1:15
67      tempF = F2((iter*tempn):((iter+1)*tempn)); %Values to plot
        [high(i), start] = max(tempF); %Find highest point to start plotting from for ←↩
                ↪consistency
69      start = start − 80; %Start a little bit earlier than the lowest one
        tempF = F2((iter*tempn)+start:((iter+1)*tempn)+start); %Update values to plot
71      low(i) = min(tempF);
```

```
        plot(T2(3:(tempn+3)),tempF)
73       iter = iter + 500;
    end
75 stdev(3) = std(low);
    stdev(4) = std(high);
77 legend('0' , '1' , '2' , '3' , '4' , '5' , '6' , '7' , '8', '9', '10', '11', '12', '13', '14')
    grid on
79 title('Cycle 4 to 7504, in steps of 500 iterations', 'Fontsize', 15)
    xlabel('Time (s)', 'Fontsize', 15)
81 ylabel('Tensional force (N)', 'Fontsize', 15)
    hold off
83
    %%
85
    iter = ceil(max(T2)/16);% − 4500; %Number of total iterations to plot, fewer for broken ↩
        ↪data
87
    tempF = zeros(1, tempn);
89
    for i=1:1:(iter)
91       if ((i+1)∗tempn) > length(F2)
             break
93        end
        tempF = F2((i∗tempn):((i+1)∗tempn));
95       [high(i), highindex] = max(tempF);
        if high(i) < 15
97           break
        end
99       if high(i) > 26 ∥ high(i) < 16
             high(i) = high(i−1);
101       end
        y(i) = high(i);
103       x(i) = i; %Use if data is unbroken
        %x(i) = T2((i∗tempn)+highindex)/16; %Use for broken data
105 end

107 n = length(y);
    i=1;
109 while i<(n−100)
        stdev(i+4) = std(x(i:i+100));
111       i=i+100;
    end
113
    figure(4)
115 % FITTED CURVE
    FT = 'exp2';
117 x = transpose(x);
    y = transpose(y);
119 [f, goodness] = fit(x,y,FT);
```

```
      plot(f, x, y);
121  hold on;
      legend('Maximum values' , 'Fit line')
123  axis([0 12000 18 23]) %Define plot limits for consistency
      grid on
125  title('Maximum values over all iterations', 'Fontsize', 15)
      xlabel('Iteration no.', 'Fontsize', 15)
127  ylabel('Tensional force (N)', 'Fontsize', 15)
      %
129  % for i=1:1:(n/100−1)
      % export(i) = mean(y(i∗100:(i∗100+100)));
131  % end

133  %export = transpose(export);
      export = y;
135  end
```
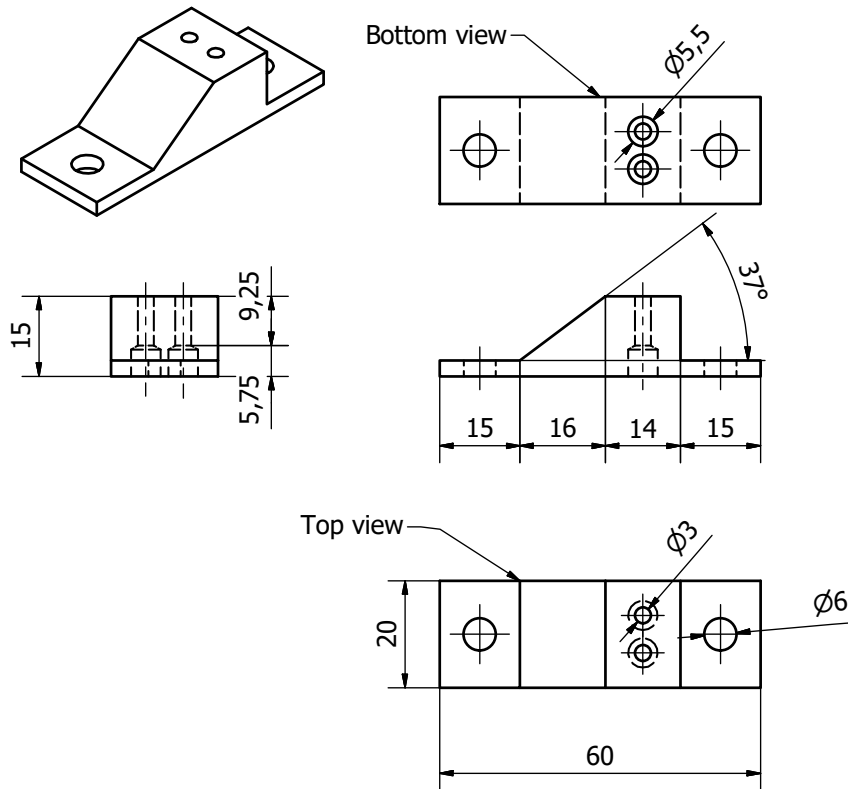
Appendix B

Schematics & Datasheets

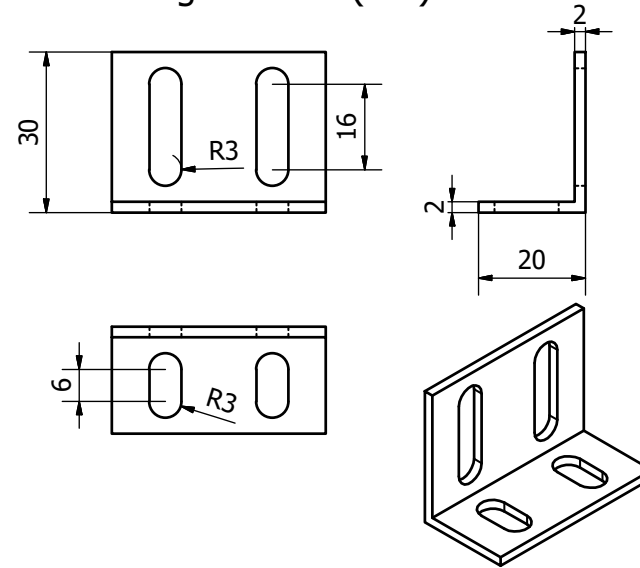The following documents are included:

1. Assembly diagram with a detailed bill of materials

2. Complete schematics of the necessary custom parts

3. Data sheet for the Load cell used

4. Specifications of the material properties of the carbon tube used

PARTS LIST

ITEM	QTY	PART NUMBER	DESCRIPTION
1	1	MiniTec Profile 30x30	Base profile; 0,6m length
2	2	MiniTec Profile 30x30	Side profile; 0,25m length
3	1	MiniTec Link 30 F/S	Hinge for the carbon tube lever arm
4	1	MiniTec Adapter 30x30 / G32	Adapter between square and circular profile
5	1	MiniTec Handle profile 32	Vertical profile; 0,5m length
6	1	SMA spring	Adaptable test subject
7	4	MiniTec Square-Nut 30 M08	Square nut for the profile
9	1	Load cell fixture	Mounting for load cell onto profile
10	1	VPG Transducers model 1006	Load cell
11	1	Goodwinds 100130	Pultruded Carbon Tube
13	1	Load cell axle part 2	
15	1	Load cell axle part 1	
16	2	Carbon tube fixture	
17	4	Angle fixture	
18	1	Load cell axle part 3	
19	1	Spring fixture	
20	16	AS 1237 - 6	Flat metal washers for general engineering purposes (metric series)
21	1	AS 1237 - 8	Flat metal washers for general engineering purposes (metric series)
22	1	AS 1110 - M6 x 16	ISO metric hexagon precision bolts and screws
23	10	AS 1110 - M6 x 12	ISO metric hexagon precision bolts and screws
24	4	AS 1427 - M3 x 12	Pozidriv ISO metric machine screws
25	4	Minitec Stopper 30	Rubber mounts added for damping

Test frame assembly (1:8)

A (1 : 4)

Load cell fixture (1:2)

Bottom view

Ø5,5

15
9,25
5,75

37°

15 16 14 15

Top view

Ø3

Ø6

20

60

Angle fixture (1:2)

2

30

16

R3

2

20

6

R3

Spring fixture (1:2)

3

7

Ø3 -3 DEEP

24

43

Designed by	Checked by	Approved by	Date	Scale	Date
Sævar Örn Einarsson				1:2	15.08.2016

HÁSKÓLINN Í REYKJAVÍK
REYKJAVIK UNIVERSITY

Custom parts 1

| VT LOK 1012 | Edition | Sheet 2 / 3 |
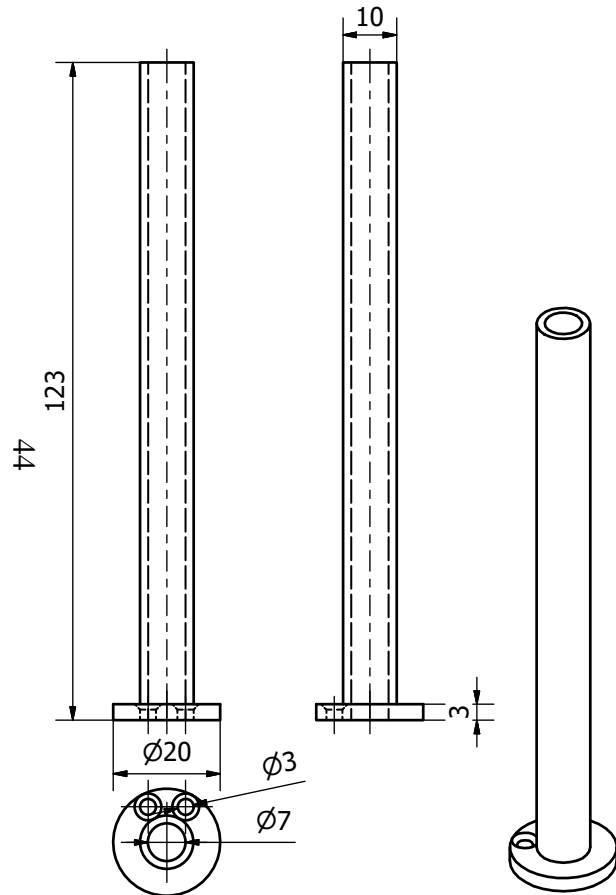
Load cell axle part 1 (1:2)

10

123

44

Ø20

Ø3

Ø7

3

Load cell axle part 2 (1:2)

12

120

10

Ø20

Ø10

R2

Load cell axle part 3 (1:2)

Ø4 -11 DEEP

10

Ø22

Ø3 -10 DEEP
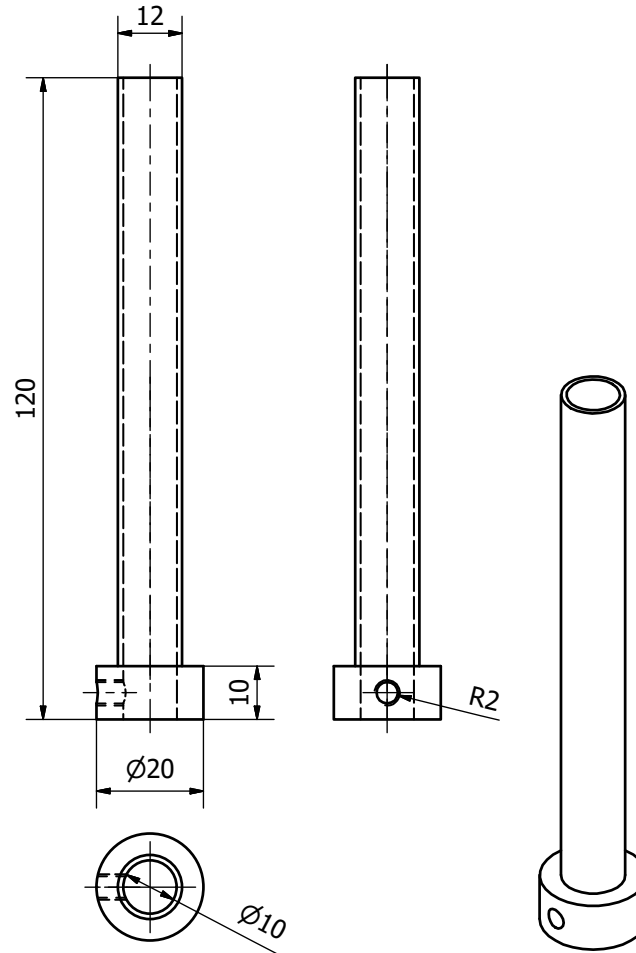
Ø12
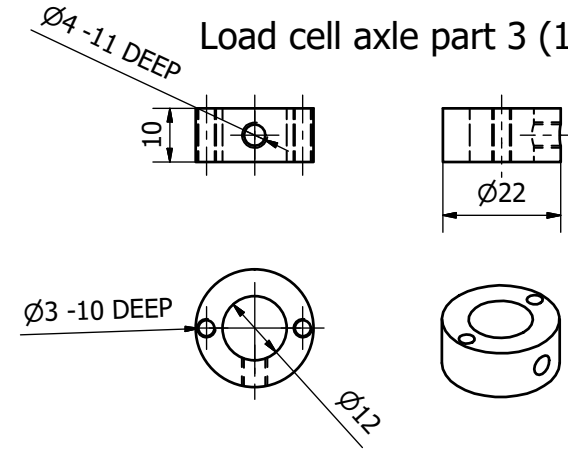
Carbon tube fixture (1:2)
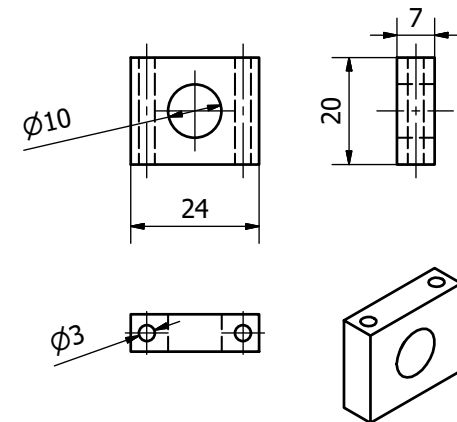
7

20

Ø10

24

Ø3

Designed by	Checked by	Approved by	Date	Scale	Date
Sævar Örn Einarsson				1:2	15.08.2016

HÁSKÓLINN Í REYKJAVÍK
REYKJAVIK UNIVERSITY

Custom parts 2

VT LOK 1012

Edition

Sheet
3 / 3

Aluminum Single-Point Load Cell

FEATURES

- Capacities 2–5 kg
- Aluminum construction
- Single-point 200 x 200 mm platform
- IP66 protection

APPLICATIONS

- Bench scales
- Counting scales
- Grocery scales

DESCRIPTION

Model 1006 is a very low capacity, high precision single-point load cell designed for direct mounting in low capacity scales.

This load cell is suitable for applications including postal scales, counting scales, general-purpose weighing scales and is also suitable for a wide variety of force measurement applications, such as industrial process control or specialist medical devices.

Model 1006 offers very high performance from a very small size. It is very easy to use, and easy to apply in a wide variety of applications, where the acting center of force application is within 100 mm of the load cell vertical axis.
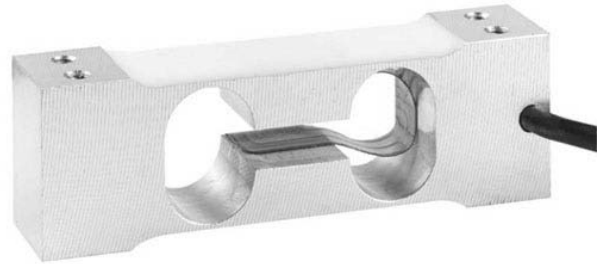
OUTLINE DIMENSIONS in millimeters

70

12

Silicone Coating

22

4-M3 through Threads

4PL

6

15

16

Model 1006

Tedea-Huntleigh

VPGTransducers

Celtron • Revere • Sensortronics • Tedea-Huntleigh
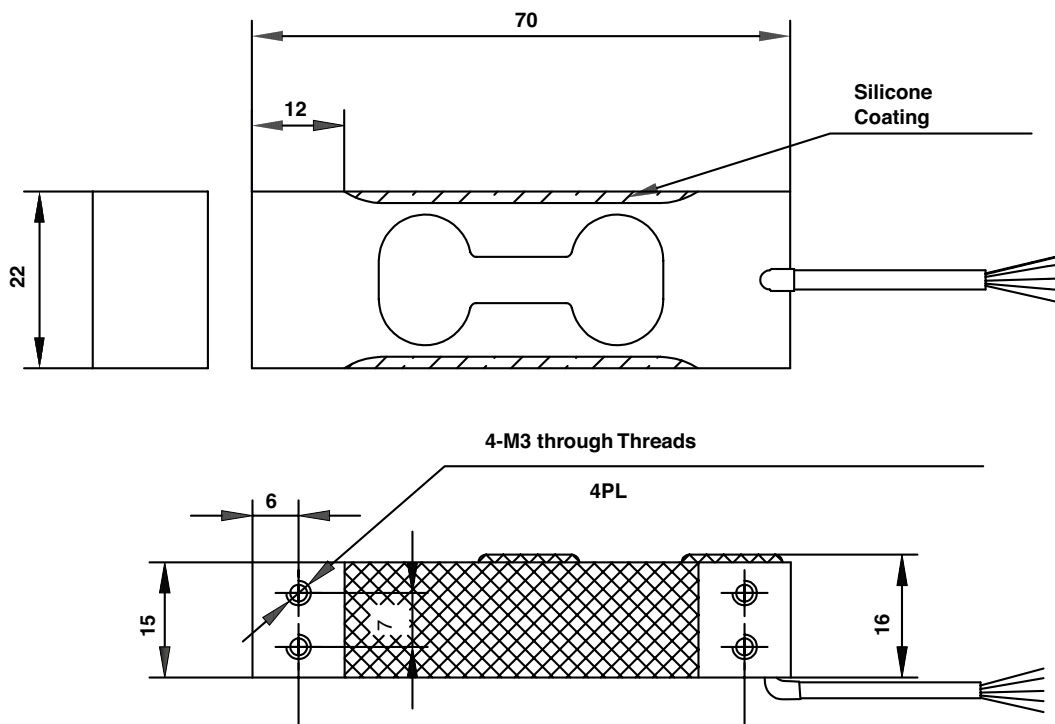
Aluminum Single-Point Load Cell

| SPECIFICATIONS			
PARAMETER	**VALUE**		**UNIT**
Accuracy class	Non-Approved	G	
Maximum no. of intervals (n)	1000	3000	
Rated capacity—R.C. (E_{max})	2, 3, 5		kg
Rated output—R.O.	2.0		mV/V
Rated output tolerance	0.2		±mV/V
Zero balance	0.2		±mV/V
Zero return, 30 min.	0.050	0.0170	±% of applied load
Total error	0.0300	0.0200	±% of rated output
Temperature effect on zero	0.0100	0.0040	±% of rated output/°C
Temperature effect on output	0.0030	0.0010	±% of load/°C
Eccentric loading error	0.0085	0.0057	±% of rated load/cm
Temp. range, compensated	−10 to +40		°C
Temp. range, safe	−20 to +70		°C
Maximum safe central overload	150		% of R.C.
Ultimate central overload	300		% of R.C.
Excitation, recommended	10		VDC or VAC RMS
Excitation, maximum	15		VDC or VAC RMS
Input impedance	415±20		Ω
Output impedance	350±3		Ω
Insulation resistance	>2000		MΩ
Cable length	0.4		m
Cable type	4 wire, PVC, single floating screen		Standard
Construction	Aluminum		
Environmental protection	IP66		
Platform size (max)	200 x 200		mm
Recommended torque	2 and 3 kg: 4.0 5 kg: 6.0		N*m

All specifications subject to change without notice.

Wiring Schematic Diagram
(Unbalanced bridge configuration)

+ve Input (Green)

+ve Output (Red)

−ve Input (Black)

−ve Output (White)
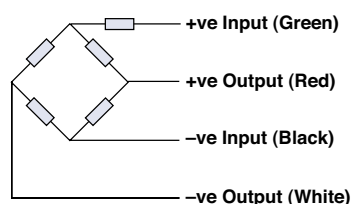
Carbon Rod

Minimum Properties	Carbon Rods < .156"	
	Standard Modulus	**Intermediate Modulus**
Tensile Strength	320 ksi / 2.34 GPa	400 ksi / 3.10 GPa
Tensile Modulus	19.5 msi / 134 GPa	24.5 msi / 169 GPa
Compressive Strength	270 ksi / 1.90 GPa	340 ksi / 2.65 GPa
Compressive Modulus	19.0 msi / 131 GPa	24.0 msi / 165 GPa
Fiber Volume	65%	65%
Ultimate Tensile Strain	1.30%	1.40%
Diameter Tolerance	+/-5%	+/-5%
Glass Transition Temperature	100° C	100° C
Matrix Material	Bis F Epoxy	Bis F Epoxy

Stock Products	Diameter	Weight
	(inch / mm)	(lbs/1000 ft. / grams/meter)
Standard Modulus	.019 / 0.48	0.37 / .55
Standard Modulus	.027 / 0.69	0.37 / .55
Standard Modulus	.037 / 0.94	0.74 / 1.10
Standard Modulus	.052 / 1.32	1.48 / 2.20
Standard Modulus	.063 / 1.60	2.22 / 3.30
Standard Modulus	.098 / 2.49	5.19 / 7.72
Standard Modulus	.125 / 3.18	8.90 / 13.24
Standard Modulus	.156 / 3.96	13.34 / 19.85

Minimum Properties	Carbon Rods > .156"
Tensile Strength	250 ksi / 1.72 GPa
Tensile Modulus	20.0 msi / 138 GPa
Ultimate Shear Strength	6.0 ksi / 41.3 Mpa
Ultimate Tensile Strain	1.50%
Flexural Strength	265 ksi / 1.83 GPa
Flexural Modulus	19.0 msi / 131 GPa
Fiber Volume	62%
Thermal Expansion Coefficient	-0.1 ppm/cm^3 / -0.2 ppm/°C
Density	.054 lbs/in^3 / 1.5 g/cm^3
Diameter Tolerance	+.000 / -.005"
Glass Transition Temperature	100° C
Matrix Material	Bisphenol Epoxy Vinyl Ester

School of Science and Engineering
Reykjavík University
Menntavegur 1
101 Reykjavík, Iceland
Tel. +354 599 6200
Fax +354 599 6201
www.ru.is